CHALMERS
UNIVERSITY OF TECHNOLOGY

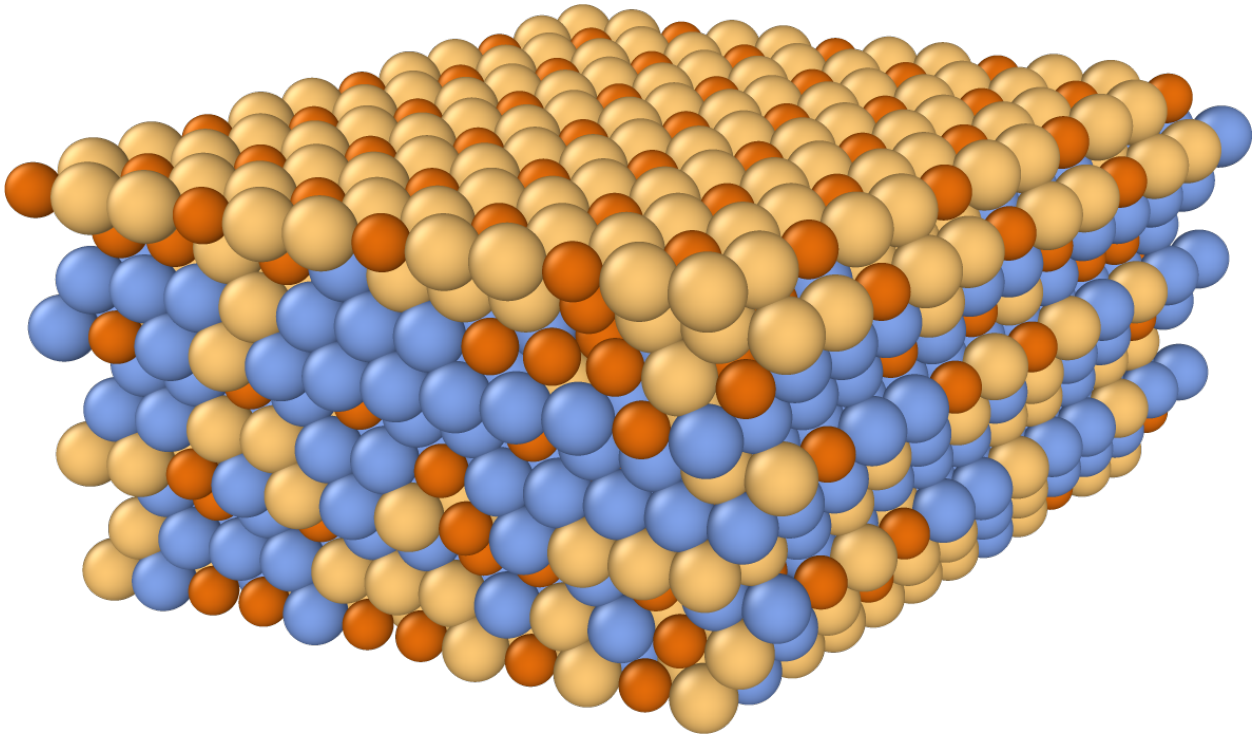

Ordering and segregation in the PdAuCu system:

Bulk vs. surface

Master's thesis in Applied Physics

PERNILLA TANNER

Department of Physics
CHALMERS UNIVERSITY OF TECHNOLOGY
Gothenburg, Sweden 2019

Master's thesis 2019

Ordering and segregation in the PdAuCu system:

Bulk vs. surface

PERNILLA TANNER

CHALMERS
UNIVERSITY OF TECHNOLOGY

Department of Physics
Division of Materials and Surface Theory
Chalmers University of Technology
Gothenburg, Sweden 2019

Ordering and segregation in the PdAuCu system:
Bulk vs. surface
PERNILLA TANNER

Examiner and supervisor: Paul Erhart, Department of Physics

Master's Thesis 2019
Department of Physics
Division of Materials and Surface Theory
Chalmers University of Technology
SE-412 96 Gothenburg
Telephone +46 31 772 1000

Cover: An fabricated illustration of surface segregation in the PdAuCu system.

Typeset in LaTeX
Printed by Chalmers Reproservice
Gothenburg, Sweden 2019

Ordering and segregation in the PdAuCu system:
Bulk vs. surface
PERNILLA TANNER
Department of Physics
Chalmers University of Technology

Abstract

Nanoalloys are of interest in many fields of research such as catalysis, sensing and energy storage. They are, however, challenging to model due to the large number of available atomic configurations. In this thesis, the first-principle based method of cluster expansion is used to study atomic ordering and surface segregation of the PdAuCu system. It is shown that under vacuum conditions, Au shows a pronounced tendency to segregate towards the surface in relation to both Cu and Pd, while the CuPd system shows a slight excess of Pd at the surface. In addition, it is found that the AuCu system as well as the full AuCuPd system exhibit phase segregation in bulk due to several ordered phases, while AuPd and CuPd show complete miscibility.

Keywords: palladium, Pd, gold, Au, copper, Cu, Cluster expansion, surface segregation, ordering

Acknowledgements

First and foremost I would like to thank Prof. Paul Erhart, my examiner and supervisor, for all of your help and support during this thesis work. Your immense knowledge, drive and vision is inspiring and I look forward to learning from you for five more years as a PhD student.
I would also like express my sincerest gratitude to all members of the Computational Materials group at Chalmers for providing a fun and stimulating atmosphere where help can always be found. In particular, to Magnus Rahm for sharing your invaluable insights in cluster expansion of alloys and to Joakim Löfgren for acting as my personal VASP support.
Lastly, I want to thank Olof Ekborg for your love and support, my family for always believing in me, and my friends for making the last five years the best of my life.

Pernilla Tanner, Gothenburg, June 2019

Contents

Acronyms

ARDR automatic relevance detection regression. 5, 15, 18, 19, 21

CE cluster expansion. 2, 3, 5, 8, 11–19, 21–23, 25–27, 29, 33, 34, 40, 41
CV cross-validation. 5, 14, 15, 17, 18, 20–22, 25, 33

DFT density functional theory. 1, 3, 6–8, 13, 18–22, 25–27, 33, 34

EAM embedded atom method. 13, 17–23, 36, 41
ECIs effective cluster interactions. 4, 5, 14, 15, 17, 18, 25, 33, 40

LASSO least absolute shrinkage and selection operator. 5, 18

MC Monte Carlo. 3, 5, 8–10, 12, 14–16, 20, 22, 28–30, 32, 35–39, 41

OLS ordinary least-squares. 5, 18

RFE recursive feature elimination. 5, 18
RMSE root mean square error. 5, 14, 17, 18, 20–22, 25, 33

SGC semi-grand canonical. 9, 10, 16, 29–32

VCSGC variance-constrained semi-grand canonical. 10, 16, 28–30, 35

1
Introduction

Metallic nanoparticles are of interest both in fundamental research and for applications in catalysis [1, 2], energy storage [3, 4], and hydrogen sensing [5, 6]. The appeal of nanoparticles is multifaceted. First, nanoparticles offer a higher surface-to-volume ratio than conventional materials by definition, since a large fraction of the atoms are at the surface. Second, many material properties change with nanoparticle size and shape, with both scalable and non-scalable regimes, which opens up for new degrees of freedom [7–9]. Third, many nanomaterials exhibit interesting optical properties, including their plasmonic response [10, 11], suitable for a range of sensing applications.

In essence, nanoengineering is one way to expand the space of design parameters in the material design process, which can be crucial when optimizing a system for a certain application. Another approach is to introduce more than one species. The number of existing elements is finite, which poses a constraint in material design. Naturally, by considering multicomponent systems the available scope of materials increases. The combination of these two approaches, resulting in nanoengineered multicomponent systems, enables tuning of material properties and, in principle, the ability to tailor materials for specific applications.

Parallel to this development is the increasing importance of computational methods in materials science. Ab initio techniques such as density functional theory (DFT), which enable a quantum mechanical description of a system, have become standard procedure in many fields of research. Accurate modelling of physical systems provides means to scan a larger portion of the space of design parameters, since the time and resource-expensive process of synthesis and characterization can be limited to the candidate systems with most promise.

An unavoidable paradox is that as the system considered becomes more complex, by nanoengineering and/or expanding the number of components, the modelling becomes increasingly complicated. The consequence is a compromise between approximations in the computational model and the size of the parameter space considered. To fully take advantage of the possibilities provided by large parameter spaces and ab initio calculations, smart modelling schemes are necessary, which is where this thesis takes off.

1.1 Pd-based nanoparticles for hydrogen sensing

An example of a nanoengineered multicomponent system can be found in the field of nanoplasmonic hydrogen sensing. Given the urgent demand for non-fossil fuels,

hydrogen has emerged as a candidate due to its high gravimetric energy density and natural abundance. Since hydrogen is highly explosive and challenging to store, efficient hydrogen sensing techniques are needed to detect potential leaks in order to enable safe hydrogen fueled vehicles.

Nanoplasmonic hydrogen sensing is a technique where localized surface plasmon resonance (LSPR) of metal nanoparticles is used to measure the amount of hydrogen in the surrounding environment [6]. A candidate nanoparticle material is Pd due to its favourable plasmonic, thermodynamic and kinetic properties during hydrogen absorption and desorption [5, 12]. Pd nanoparticles show, however, hysteresis when measuring hydrogen absorption and desorption as well as a tendency for CO poisoning [12, 13]. To solve these problems, the introduction of a second alloying element such as Au or Cu has been suggested. Both the PdAu and the PdCu systems can be tuned to eliminate hysteresis, but the introduction of Au does not improve CO poisoning while Cu solves the CO poisoning but strongly reduces the sensitivity of the nanoplasmonic sensor [12, 13]. A natural next step is to investigate the ternary PdAuCu system, which has shown promise in solving the above mentioned problems without sacrificing sensitivity [13].

A common issue with nanoparticle alloys is surface segregation [14]. Since the surface constitutes the interface to the surrounding environment, its composition is crucial. In the case of Pd-based nanoplasmonic hydrogen sensing, the surface composition greatly affects the hydrogen sorption kinetics [13]. Therefore, in order to develop long-lived plasmonic hydrogen sensors, it is of interest to study the ordering and segregation of atoms in nanoalloys, such as the PdAuCu system.

1.2 Thesis objective and limitations

This thesis is devoted to studying the thermodynamic ordering and surface segregation of the PdAuCu system at various concentrations. The work is purely computational and focused on the issue posed by the extremely large configuration space associated with binary and ternary systems, with a method based on the cluster expansion (CE) technique [15, 16]. The aim is to produce results, such as phase diagrams and surface segregation profiles, that provide a theoretical basis for design rules of PdAuCu nanoparticles for nanoplasmonic hydrogen sensing. The results are also of general interest since the methods could easily be generalized to any multicomponent bulk or surface system.

The thesis work is limited to studies of bulk and surface of the PdAuCu system, rather than nanoparticles. This is motivated by the fact that in sensing applications, nanoparticles are typically on the 100 nm-scale [13], where bulk and surface sites dominate as opposed to edge and corner sites. All systems studied have FCC crystal structure and all surfaces are in (111) direction. In addition, the system will be studied in vacuum neglecting the interactions with hydrogen or other adsorbates.

The thesis will be structured as follows. In Chapter 2, the necessary background theory is covered. Then, in Chapter 3, the methodology of the thesis work is presented. Chapter 4 is devoted to passing on the insights obtained on how to design and evaluate a CE. The following chapters, Chapter 5 and 6, are focused on results related to bulk and surfaces, respectively. Lastly, Chapter 7 concludes the thesis.

2

Theory

This chapter introduces the computational methods used in this thesis, starting with the most important method, CE, which enables ab initio based studies of multicomponent systems. Then, the basis of DFT is explained which is a key method for providing the necessary training data for CE construction. Lastly, Monte Carlo (MC) simulation, which is used for thermodynamic sampling of a CE, is covered.

2.1 Cluster expansion

Before describing the CE formalism, it is instructive to introduce a few key concepts.

The atomic configuration of a crystalline material can be described by the configuration vector

$$\boldsymbol{\sigma} = \{\sigma_1, \sigma_2, ..., \sigma_N\},$$

where σ_i is a number describing what species occupies lattice site i and N is the total number of atoms in the unit cell. For a ternary system, σ_i can be defined as 0 for species A, 1 for species B and 2 for species C.

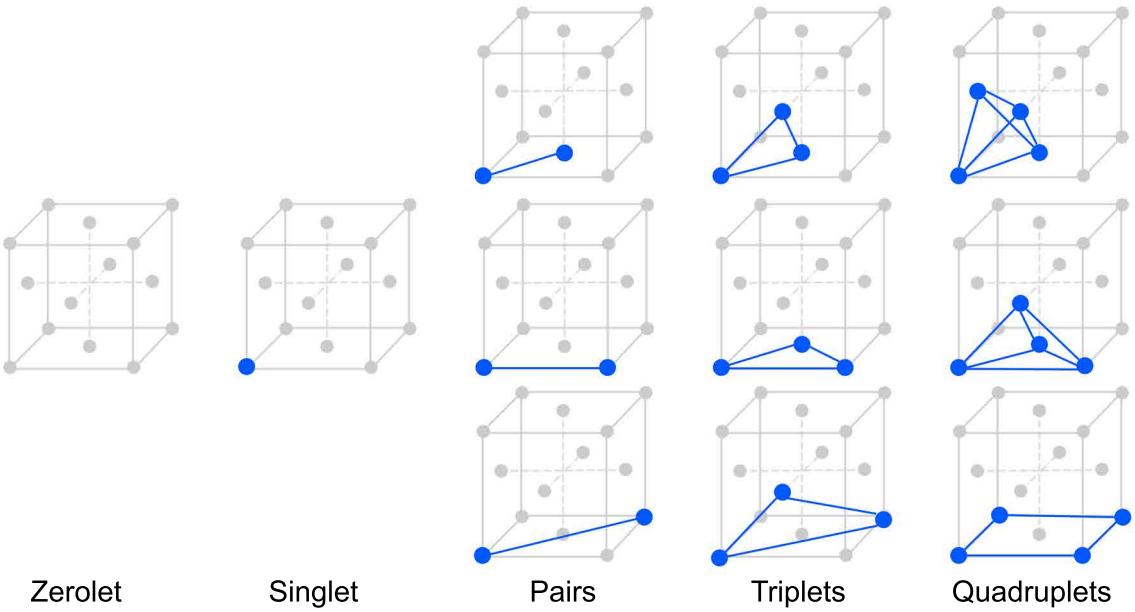

Figure 2.1: An overview of clusters on a FCC lattice. Each column represents a certain order, where zerolets are order 0, singlets are order 1 and so on.

A cluster is defined as a set of k lattice sites. Clusters can be classified by order, which is the number of sites k, and by radius, which is the average distance between cluster sites and the geometric center of mass of the cluster. Examples of clusters of order 0–4 on a FCC lattice is shown in Fig. 2.1. Clusters obey the symmetry of the lattice, and a group of clusters that can be turned into each other by allowed symmetry operations are said to belong to the same orbit.

For each lattice site i, a set of M so called point functions $\Theta_n(\sigma_i)$ can be defined as

$$\Theta_n(\sigma_i) = \begin{cases} 1, & n = 0 \\ -\cos\left(\frac{\pi(n+1)\sigma_i}{M}\right), & n \text{ odd} \\ -\sin\left(\frac{\pi n\sigma_i}{M}\right), & n \text{ even} \end{cases}$$

where M is the number of allowed species on a site, for example $M = 3$ in a ternary alloy, and $n = 0, 1, .., M-1$ is the point function index.

These point functions can be used to construct an orthogonal basis that is complete in the configuration space [16] with basis functions

$$\Pi_{\boldsymbol{\alpha}}(\boldsymbol{\sigma}) = \Theta_{n_1}(\sigma_1)\Theta_{n_2}(\sigma_2)\cdots\Theta_{n_l}(\sigma_l),$$

where l is the total number of lattice sites and $\boldsymbol{\alpha} = \{n_1, n_2, ..., n_l\}$ is a vector where element n_i represents lattice site i. For a specific cluster, $n_i = 0$ for all sites i not included in the cluster and $n_i = 1, 2, ..., M-1$ for sites included in the cluster. This notation is convenient since $\Theta_0(\sigma_i) = 1$, meaning that sites not included in a cluster $\boldsymbol{\alpha}$ will not affect the corresponding basis function $\Pi_{\boldsymbol{\alpha}}(\boldsymbol{\sigma})$.

The CE formalism is based on the fact that if an orthogonal basis of the configuration space with basis functions $\Pi_{\boldsymbol{\alpha}}(\boldsymbol{\sigma})$ can be found, then any function f of the configuration (such as the energy) can be expressed as [17]

$$f(\boldsymbol{\sigma}) = f_0 + \sum_{\boldsymbol{\alpha}} f_{\boldsymbol{\alpha}}\Pi_{\boldsymbol{\alpha}}(\boldsymbol{\sigma}),$$

where f_0 corresponds to the contribution from zero-order clusters (with configuration independent basis functions since $n_i = 0$ for all sites i) and the summation is over all nonzero-order clusters $\boldsymbol{\alpha}$ of the lattice. For reasons of symmetry, the sum over all clusters can be reduced to a sum over all orbits where each orbit is represented by one of its clusters $\boldsymbol{\alpha}$ and the basis function is averaged over all clusters $\boldsymbol{\alpha}'$ in the orbit

$$f(\boldsymbol{\sigma}) = J_0 + \sum_{\boldsymbol{\alpha}} m_{\boldsymbol{\alpha}} J_{\boldsymbol{\alpha}} \left\langle \Pi_{\boldsymbol{\alpha}'}(\boldsymbol{\sigma}) \right\rangle_{\boldsymbol{\alpha}}, \tag{2.1}$$

where $m_{\boldsymbol{\alpha}}$ is the multiplicity of clusters in the orbit represented by $\boldsymbol{\alpha}$ and effective cluster interactions (ECIs) $J_{\boldsymbol{\alpha}}$ has been introduced.

2.1.1 Cluster expansion construction

In practice, a CE is constructed by using reference data $\boldsymbol{f} = [f_1(\boldsymbol{\sigma}_1), f_2(\boldsymbol{\sigma}_2), ...]^T$ at some arbitrary configurations $\{\boldsymbol{\sigma}_1, \boldsymbol{\sigma}_2, ...\}$, usually obtained by ab initio calculations.

Equation (2.1) can then be written as a matrix equation

$$\boldsymbol{f} = \boldsymbol{\Pi J} \tag{2.2}$$

where the sum over $\boldsymbol{\alpha}$ has been truncated to only include orbits of clusters below some cutoff radius r_{cutoff}. The truncation is motivated by the fact that physical interactions are generally short-ranged, meaning that larger clusters will have a less significant contribution. The vector $\boldsymbol{J} = [J_0, J_1, J_2, ...]^T$ holds the ECIs of all non-truncated orbits and each row $\boldsymbol{\Pi}_i$ of the sensing matrix $\boldsymbol{\Pi}$ corresponds to the multiplicity and averaged basis function of all non-truncated orbits

$$\boldsymbol{\Pi}_i = [1, \left\langle \Pi_{\boldsymbol{\alpha}_1'}(\boldsymbol{\sigma}_i) \right\rangle_{\boldsymbol{\alpha}_1} m_{\boldsymbol{\alpha}_1}, \left\langle \Pi_{\boldsymbol{\alpha}_2'}(\boldsymbol{\sigma}_i) \right\rangle_{\boldsymbol{\alpha}_2} m_{\boldsymbol{\alpha}_2}, ...].$$

Equation (2.2) is a linear system of equations that, if solved, provides the ECIs for all non-truncated orbits. The ECIs can then be inserted into Eq. (2.1), providing a CE of the system that enables calculation of f for any configuration $\boldsymbol{\sigma}$.

In general, the length of $\boldsymbol{f}$ and $\boldsymbol{J}$ is not the same, resulting in an over or underdetermined system, which calls for linear regression techniques to find $\boldsymbol{J}$ that minimizes $\|\boldsymbol{\Pi J} - \boldsymbol{f}\|_2$. Examples of linear regression techniques used for CE are ordinary least-squares (OLS), least absolute shrinkage and selection operator (LASSO), recursive feature elimination (RFE) and automatic relevance detection regression (ARDR) [15]. These solution techniques may well be combined with cross-validation (CV) to improve and evaluate the CE. CV consists of splitting the reference data into one training and one validation set, where the former is used to fit ECIs and the latter to calculate the CV root mean square error (RMSE) of the CE as

$$\text{CV-RMSE} = \sqrt{\frac{1}{N}\sum_{i=1}^{N}\left(f^{CE}(\boldsymbol{\sigma_i}) - f(\boldsymbol{\sigma_i})\right)^2}$$

where N is the number of configurations $\boldsymbol{\sigma_i}$ in the validation set, f^{CE} is the function value calculated from the CE and f is the function value from the reference data. This process can be repeated with different splits, until an optimized CE is found.

2.1.2 Sampling the cluster expansion

Once a CE is constructed, it can be used as a function for determining the mixing energy of any atomic configuration of a system with the same lattice structure and species. This opens up for ab initio based studies of systems that are too large and/or have too large configuration spaces to be feasible to study with ab initio methods alone.

A CE can be sampled with MC simulations where the CE is used to calculate the mixing energy in each step of the simulation. This allows for calculation of macroscopic quantities such as the free energy of mixing as a function of the concentration at varying temperature, which is crucial in determining phase diagrams.

2.2 Density functional theory

In several fields of research it is of interest to calculate the quantum mechanical ground state of many-body systems. This is, for most realistic systems, a complicated task that requires advanced computational methods. The most widely used such method is DFT. For the purpose of this thesis, DFT calculations are performed to generate the reference data $\boldsymbol{f}$ in Eq. (2.2). This section provides the theory behind DFT, based on Ref. [18].

2.2.1 The Hohenberg-Kohn theorems

The Hamiltonian for the electrons of a many-body system with fixed nuclei can be written as

$$\hat{H} = -\frac{\hbar^2}{2m_e}\sum_i \boldsymbol{\nabla}_i^2 + \sum_i V_{\text{ext}}(\mathbf{r}_i) + \frac{1}{2}\sum_{i\neq j}\frac{e^2}{|\mathbf{r}_i - \mathbf{r}_j|},$$

where the first term is the kinetic energy, the second is due to an external potential $V_{\text{ext}}(\mathbf{r})$ (including the effect of the fixed nuclei) and the last is the Coulomb interaction between electrons. The nuclei are regarded as fixed in accordance with the Born-Oppenheimer approximation.

For most real systems, it is not feasible to solve the corresponding Schrödinger equation, which is where DFT enters. The base of DFT is the following two theorems and their corollaries proved by Hohenberg and Kohn in 1964 [19].

Theorem I: The external potential $V_{\text{ext}}(\mathbf{r})$ is uniquely determined by the ground state particle density $n_0(\mathbf{r})$

Corollary I: The many body wavefunctions for all states, and therefore all properties of the system, are completely determined by the ground state particle density $n_0(\mathbf{r})$.

Theorem II: For any external potential $V_{\text{ext}}(\mathbf{r})$, a universal functional $E[n]$ for the energy of the density can be defined. The global minimum of this functional is the ground state energy of the system and the corresponding density is the ground state particle density $n_0(\mathbf{r})$.

Corollary II: The functional $E[n]$ is sufficient to determine the exact ground state energy and density.

What these theorems mean in practice is that the problem of finding the ground state of a system is reduced from solving the Schrödinger equation to minimizing some functional of the particle density. They provide, however, no guidance on how to find said functional.

A general expression for the energy functional is

$$E_{\text{HK}}[n] = T[n] + E_{\text{int}}[n] + \int \mathrm{d}\mathbf{r} V_{\text{ext}}(\mathbf{r})n(\mathbf{r}) + E_{II}, \tag{2.3}$$

where T and E_{int} are the kinetic and internal energy contributions of the interacting electrons and E_{II} is the interaction energy of the nuclei.

2.2.2 The Kohn-Sham ansatz

In most DFT implementations, the Kohn-Sham ansatz [20] is used. The main idea is to replace the many-body problem by an auxiliary independent-particle problem that is easier to handle. The underlying assumption is that the independent-particle problem can be defined such that both problems share the same ground state.

The Hamiltonian for an electron in the auxiliary system is

$$\hat{H}_{\text{KS}} = -\frac{\hbar^2}{2m_e}\boldsymbol{\nabla}^2 + V_{\text{KS}}(\mathbf{r})$$

where $V_{\text{KS}}(\mathbf{r})$ is the effective Kohn-Sham potential, which will be explained later. If the corresponding Schrödinger equation,

$$\hat{H}_{\text{KS}}\phi_i(\mathbf{r}) = \epsilon_i\,\phi_i(\mathbf{r}), \tag{2.4}$$

can be solved, the ground state density for a system of N electrons can be identified as

$$n_0(\mathbf{r}) = \sum_{i=1}^{N} |\phi_i(\mathbf{r})|^2$$

where ϕ_i are the N eigenvectors with lowest corresponding eigenvalue ϵ_i.

The energy functional Eq. (2.3) of the interacting many-body problem can be rewritten in terms of the auxiliary problem as

$$E_{\text{KS}}[n] = T_{\text{KS}}[n] + \int \mathrm{d}\mathbf{r} V_{\text{ext}}(\mathbf{r})n(\mathbf{r}) + E_{II} + E_{\text{Hart}}[n] + E_{\text{xc}}[n] \tag{2.5}$$

where T_{KS} is the kinetic energy contribution in the auxiliary system. $E_{\text{Hart}}[n]$ is the Hartree energy,

$$E_{\text{Hart}}[n] = \frac{e^2}{2}\int \mathrm{d}\mathbf{r}\mathrm{d}\mathbf{r}'\frac{n(\mathbf{r})n(\mathbf{r}')}{|\mathbf{r}-\mathbf{r}'|},$$

which is the Coulomb interaction energy in terms of electron density. The many-body effects are grouped into the exchange-correlation functional $E_{\text{xc}}[n]$. The physical meaning of the exchange-correlation functional is the difference in kinetic and internal energy of the electrons in the auxiliary and interacting systems, but in practice it has to be approximated.

The effective Kohn-Sham potential $V_{\text{KS}}(\mathbf{r})$ is found by minimizing the energy functional in Eq. (2.5) with the Lagrange multiplier method, which yields

$$V_{\text{KS}}(\mathbf{r}) = V_{\text{ext}}(\mathbf{r}) + \frac{\delta E_{\text{Hart}}}{\delta n(\mathbf{r})} + \frac{\delta E_{\text{xc}}}{\delta n(\mathbf{r})} = V_{\text{ext}}(\mathbf{r}) + V_{\text{Hart}}(\mathbf{r}) + V_{\text{xc}}(\mathbf{r}).$$

Once this potential is found, the auxiliary problem in Eq. (2.4) can be solved by numerical means and the ground state energy and density can be calculated. Then, in accordance with the Hohenberg-Kohn theorems, all properties of the system are completely determined.

In most implementations, the solution of the Kohn-Sham equation Eq. (2.4) is done with a self-consistent approach. The ground state density is set to an initial guess and the Kohn-Sham effective potential is calculated. Then, the Kohn-Sham equation is solved and a new ground state density is calculated. This new ground state density is used to reiterate the process from the calculation of the Kohn-Sham effective potential, and this loop is continued until the ground state density converges.

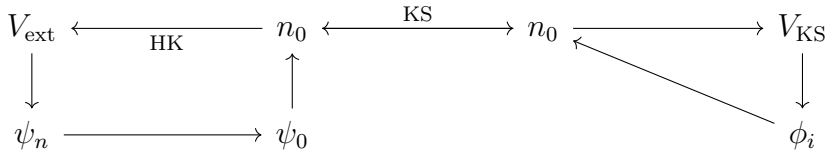

(2.6)

Equation (2.6) shows a schematic overview of the principle of DFT. The right side shows the self consistent Kohn-Sham loop of the auxiliary problem where the ground state density is used to calculate the Kohn-Sham potential. The potential is used to calculate the wavefunction, which is then used to recalculate the ground state density. The left side show the corresponding flow for the interacting problem.

2.3 Monte Carlo simulation

MC methods are based on using random numbers and probabilities to navigate large configuration spaces. A common example is MC integration [21] of multi-dimensional integrals. The most straight-forward approach would be to resolve the integrand on some grid over the domain and sum the values. MC integration, on the other hand, enables a more efficient numerical scheme where the sampling points are chosen at random and weighted by their probability.

The MC approach can also be used to simulate complex physical systems and processes. The idea is to sample some trajectory, starting from an initial guess, by taking steps where the system is subjected to some random change and each step is kept or discarded based on the difference in probability before and after. In the case of CE sampling, it is the configuration of atoms that is randomly changed and the corresponding probability is based on the thermodynamic potential.

For the purpose of this thesis, each step of a MC simulation starts with a change in the atomic configuration. This can be done in a number of ways, but the most common method is the Metropolis algorithm [22], where the generation of new configurations follows a Markov chain, meaning that the new configuration has no memory of previous configurations. For any given configuration X, the probability ρ is defined as

$$\rho(X) \propto \exp\left[-\frac{\Phi(X)}{k_B T}\right] \tag{2.7}$$

where Φ is the thermodynamic potential, which will be explained in Section 2.3.1. The probability of the new configuration, $\rho(X_i)$, is compared with the probability of the old configuration, $\rho(X_{i-1})$. If $\rho(X_i) > \rho(X_{i-1})$, the new configuration is always kept. Otherwise, the probability of keeping the new configuration is $\rho(X_i)/\rho(X_{i-1})$. With this scheme, a lower energy configuration will always be kept and a higher

energy configuration might be kept, with a lower probability the higher the energy. This is convenient since it avoids getting trapped in local minima. Usually, a MC simulation contains a large number of steps and any studied observable is averaged over a large series of steps.

2.3.1 Statistical physics and thermodynamic ensembles

In order to define an appropriate thermodynamic potential $\Phi(X)$ to use in the probability expression in Eq. (2.7), knowledge in statistical physics is necessary.

Consider a system of N particles confined to a volume V in the thermodynamic limit, where N and V go to infinity while the particle density remains fixed. The total energy of the system is E, and the values of these three variables (N, V, E) define the macrostate of the system. Generally, each macrostate can be built from multiple microstates, where the microstate contains information about the state of every single particle.

As time progresses, the microstate of the system will change within the same macrostate. Thus, it is usually more interesting to study the averaged properties of the system rather than the instant microstate. This is done by introducing an ensemble, which is a collection of copies of the system in different microstates, where the microstates X are distributed according to the probability or density function $\rho(X)$. Any observable can then be studied in terms of ensemble averages. There are many ways to set up the ensemble, depending on the system in question. In the following, three ensembles relevant to this thesis will be presented.

2.3.2 The canonical ensemble

Often it is more convenient to study systems with fixed temperature T rather than energy. This is the basis of the canonical ensemble, where a macrostate is defined by (N, V, T) [23–25]. The canonical ensemble represents a physical system in contact with an infinite reservoir at constant T. The system can be extended to include different species, with N_i particles of species i. The system can exchange energy with the reservoir, but the boundaries of the system inhibit exchange of particles and change of volume, thus keeping (N_i, V, T) constant.

The probability distribution of microstates in the canonical ensemble reads

$$\rho_{\mathrm{C}}(X) \propto \exp\left[-\frac{U(X)}{k_B T}\right]$$

where U is the mixing energy of the microstate X. Since the concentrations of species are kept constant, the only driving force to change the microstate is a decrease in mixing energy. The consequence of this is that the chemical potential can not be observed, which is, as will become clear in the following sections, inconvenient when studying multicomponent systems.

2.3.3 The semi-grand canonical ensemble

In the semi-grand canonical (SGC) ensemble, the fixed thermodynamic variables are $(N, \Delta\mu_i, V, T)$, where $\Delta\mu_i = \mu_1 - \mu_i$ is the difference in chemical potential between

species 1 and the other species [24, 25]. The physical representation is a system in contact with an infinite reservoir with fixed temperature and chemical potentials, such that both energy and particles can be exchanged. The probability distribution of microstates in the SGC ensemble is

$$\rho_{\mathrm{SGC}}(X) \propto \exp\left[-\frac{U(X) + \sum_{i>1} \Delta\mu_i N_i}{k_B T}\right].$$

The difference between ρ_{SGC} and ρ_{C} is that in the SGC ensemble, there is a second driving force related to the chemical potentials of the microstate.

Within the SGC ensemble, the chemical potential can be observed, which yields the free energy derivative via the relation

$$\Delta\mu = -\frac{1}{N}\frac{\partial F}{\partial c},$$

for binary systems. This means that the free energy derivative can easily be sampled with a MC simulation, and then integrated to obtain the free energy as a function of the concentration, which is often used to determine the corresponding phase diagram. A remaining issue is that the SGC ensemble can sample single-phase regions only, since the concentration as a function of the difference of chemical potential becomes multi-valued in multi-phase regions.

2.3.4 The variance-constrained semi-grand canonical ensemble

The variance-constrained semi-grand canonical (VCSGC) ensemble is similar to the SGC ensemble but defined such that sampling across multi-phase regions is possible [24, 25]. The only difference in the physical representation is that now, the reservoir is finite, which affects the fluctuations of the thermodynamic variables.

The fixed thermodynamic variables are (N, ϕ, κ, V, T), where ϕ and κ control the average concentration and its fluctuation. The probability distribution in the VCSGC ensemble reads

$$\rho_{\mathrm{VCSGC}}(X) \propto \exp\left[-\frac{U(X) + \kappa N(c + \phi/2\kappa)^2}{k_B T}\right]$$

for a binary system. The corresponding relation for the free energy derivative is

$$\Delta\mu = -\frac{1}{N}\frac{\partial F}{\partial c} = \phi + 2N\kappa\left\langle c\right\rangle.$$

From this relation, it is clear that $\phi \to \Delta\mu$ as $\kappa \to 0$. This provides the interpretation of κ as the the (inverse) size of the finite reservoir. When $\kappa \to 0$, the reservoir becomes infinite and the VCSGC ensemble transitions into the SGC ensemble.

The free energy can be obtained from the free energy derivative with the same procedure as for the SGC ensemble, but within the VCSGC ensemble both single- and multi-phase regions can be sampled. There are methods to obtain the free energy within the canonical ensemble, but they are more complicated and less efficient [24], which is why the VCSGC ensemble is used for the majority of the MC simulations in this thesis.

3
Method

All of the work of this thesis follows the same workflow that can be divided into four steps. First, the reference structures needed to construct the CE are selected. Second, the energies of these structures are calculated to create a reference data set. Third, the CE is constructed by training against the reference data set. Lastly, the finished CE is sampled to calculate the energies of various configurations and thereby obtain information about material properties. These steps are carried out for binary and ternary bulk systems, followed by binary surfaces.

3.1 Selection of reference structures

All structures considered are FCC crystalline with different configurations of Au, Cu and Pd. In order to construct a reliable CE, the reference structures need to be selected with care. The goal is to have a sufficiently large number of reference structures that span the configuration space. In order for the numerical solution of the matrix equation to be optimal and converge quickly with the number of training structures, the sensing matrix should be well-conditioned, which essentially means that the reference structures should span the cluster space.

In bulk systems, this can be done in straightforward fashion by limiting the maximum number of atoms in the unit cell and enumerating all inequivalent configurations that can be achieved [26, 27]. The software used for CE construction and sampling, ICET [15], supports this functionality. In this thesis, bulk structures with up to 8 atoms were used, which yields 631 reference structures for binary systems and 9808 reference structures for ternary systems. The actual number of reference structures used is lower, in part due to computational difficulties in the next step leading to some structures being skipped. In addition, for the ternary bulk system, a selection of 2573 structures was done do reduce the number of calculations.

In surface systems, structure selection requires more thought. The surface structures used in this thesis are 10 layer FCC-(111) slabs with periodic boundary conditions in the surface plane and 10 Å of vacuum in the direction perpendicular to the surface. The unit cells considered have 1 to 9 atoms per layer, which yields a total of 10 to 90 atoms per unit cell. Figure 3.1 shows how the number of structures produced by enumeration increases with the number of atoms in the unit cell for bulk systems. From this analysis, one can estimate that the corresponding number for 90 atoms in a surface cell would be very large and it is not feasible to include all inequivalent configurations. A few different approaches to structure selection for surface slabs were tested, as presented in section 4.2. The method chosen is based

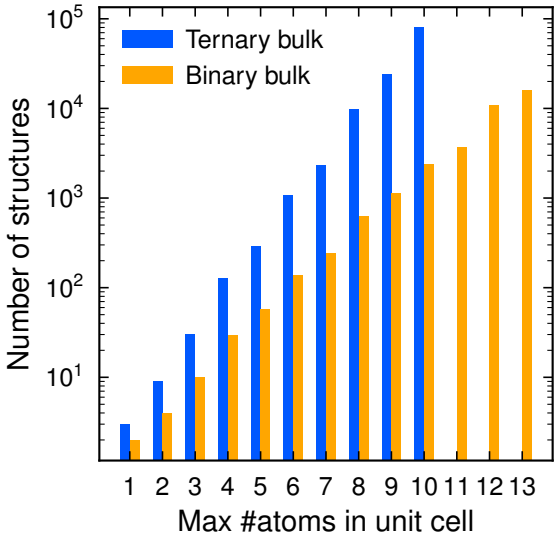

Figure 3.1: The number of structures produced by ICET enumeration as a function of the maximum number of atoms in the unit cell, for ternary and bulk FCC systems.

Concentrations	0.0	0.1	0.2	0.3	0.4	0.5	0.6	0.7	0.8	0.9	1.0
#structures	1	5	9	13	17	21	17	13	9	5	1

Dimensions	1×1	1×2	1×3	1×4	2×2	3×3

Table 3.1: A specification of the random configuration unit cells used as surface reference structures. The upper part simply presents the number of structures used for each concentration. The dimensions refer to how many multiples of the 10 layer FCC-111 primitive cell are included in the unit cell, in each direction of the surface plane.

on generating random configurations at specific concentrations, while randomly selecting the shape of the unit cell from a set of unit cells dimensions[1], see Table 3.1. To reflect the natural number of available configurations at different concentrations, a larger number of structures was generated for intermediate concentrations. The number of reference structures is lower than for the binary bulk systems, even though the configuration space is larger, because the necessary DFT calculations are more computationally expensive compared to bulk.

In addition to this approach, simulated annealing was used to extend the reference data set for the AuCu surface. A CE was constructed from the initial random structures[2] and used in MC simulations in the canonical ensemble where the temperature is decreased throughout the simulation, to simulate an annealing process. If this is done with a very large number of steps, the end configuration will be the ground state of the system. For the sake of structure selection, the simulated annealing

[1]The 3×3-cells were added at a later stage, due to ordered phases requiring a 3x3 unit cell.
[2]The 3×3-cells are not included.

was done with relatively short simulations (1000 trial steps), to generate low energy structures rather than the actual ground states. This was done 10 times for each concentration, generating a total of 90 additional structures.

3.2 Calculation of reference structure energies

The reference energies were calculated with DFT using the software VASP [28, 29] which uses a plane wave basis set [30, 31] and the projector augmented wave (PAW) method [32, 33]. The functional used is the vdW-DF-cx functional [34], with PBE pseudopotentials [32]. The calculations are done in two steps starting from ideal FCC structures. First, the unit cell and atoms are relaxed until the force is minimized, using the Methfessel-Paxton method. Then, the total energy is calculated in a final run using a denser $\boldsymbol{k}$-point mesh and the tetrahedron method.

During relaxation, the calculation is set up such that first the Kohn-Sham equations are solved for the electronic part of the problem (while the atoms are regarded as fixed). Then, the atomic positions and cell metrics are subjected to a small change and the electronic problem is solved again until forces and stresses converge. For the surface calculations, the cell metric is kept fixed at the lattice parameter found by interpolating the bulk results. For the final calculation of the total energy, the atoms are kept fixed and the electronic problem is solved again with slightly different settings appropriate for energy calculations.

The $\boldsymbol{k}$-points, which are the points on the computational grid in reciprocal space, were specified such that the minimal spacing between $\boldsymbol{k}$-points was 0.20 and 0.15 Å^{-1} for the relaxation and final calculation, respectively, and centered around the Gamma-point. The convergence criteria used were 10^{-6} eV for the electronic loop and 10 meV/Å for the ionic loop, meaning that the self-consistent loop is terminated when the difference in energy or force between two steps is below the corresponding criterion. Other computational details can be found in Appendix A where the full INCAR files of VASP input parameters are presented.

In some initial testing, embedded atom method (EAM) potentials [35, 36] were used to relax and calculate the total energy of the structures, using the software LAMMPS [37]. This approach is significantly faster at the expense of a lower accuracy compared to DFT. Since the results of these calculations will not be used for purposes other than testing and comparison, this method will not be covered in great detail.

3.3 Cluster expansion construction and validation

CE construction was carried out using the ICET software [15]. The workflow implemented in ICET, shown in Fig. 3.2, can be divided into five steps as follows.

1. A cluster space is set up, which holds information about all orbits that are to be included in the CE. In order to set up the cluster space, a few input parameters are needed. The prototype structure is a representation of the lattice structure of the system, for example the FCC primitive cell. The cutoff radii are the maximum distances between atoms of clusters to be included, for

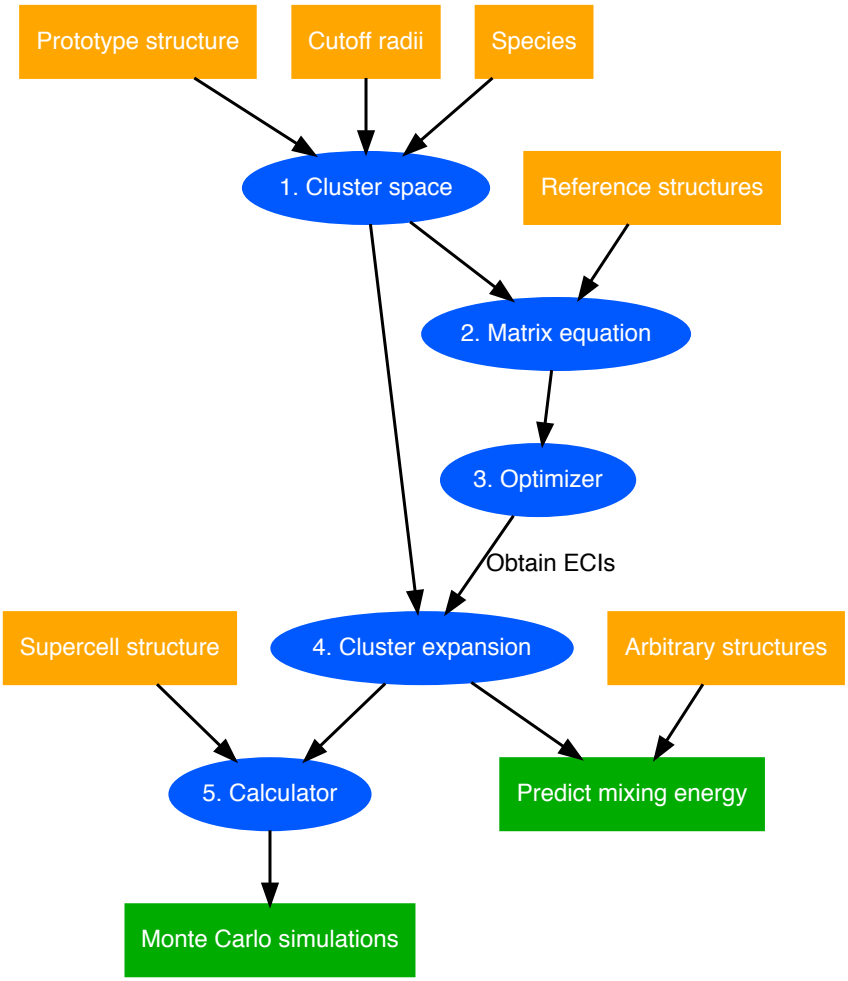

Figure 3.2: The workflow of constructing and using CEs in ICET.

each order. The species argument specifies which chemical elements are to be included in the CE.

2. The cluster space is merged with the reference data to define the matrix equation that is to be solved. For each reference structure, the values of the cluster functions are listed and the corresponding basis functions are calculated and averaged.
3. The matrix equation is numerically solved by an optimizer module that performs linear regression. This step is flexible and can either be used for training an optimal CE with the full reference data set or performing CV in a controlled manner to asses the CV-RMSE of the CE.
4. After optimization, the ECIs is extracted and a CE is constructed. The CE can be saved and used as a model to predict the mixing energy of an arbitrary structure within the same crystal structure and set of species.
5. The CE can be further used as input to a MC simulation together with a

supercell based on the same lattice structure.

The prototype structure used was a FCC primitive cell. For the bulk structures, this means a single atom with appropriate lattice vectors. For the surfaces, the primitive cell is produced by slicing out a 10 layer surface slab from a FCC lattice in the (111) surface plane. The smallest repeating unit, that is the primitive cell, is then a row of 10 atoms in the direction of the surface normal. In the bulk cluster spaces, clusters up to fourth order were included, with cutoff radii 13.0, 6.6, and 6.0 Å for pairs, triplets and quadruplets, respectively. In the surface cluster spaces, clusters up to third order were included, with cutoff radii 10.0 and 5.0 Å for pairs and triplets, respectively. The reference structure selection and associated calculations are described in Sections 3.1 and 3.2, respectively.

The optimizing step was performed with the ARDR method for the most parts. This selection is motivated in Section 4.1. Detailed CV was performed to tune the selection of hyperparameters related to linear regression and study the influence of the size of the reference data set. Then, the ECIs were extracted by training the model on the full reference data set with the optimized hyperparameters, and the final CE was constructed.

3.4 Sampling of cluster expansions

Several MC simulations were conducted in order to sample the CEs over the entire concentration range, with a larger supercell and at different temperatures. The sampling was done using the MCHAMMER module of ICET [15].

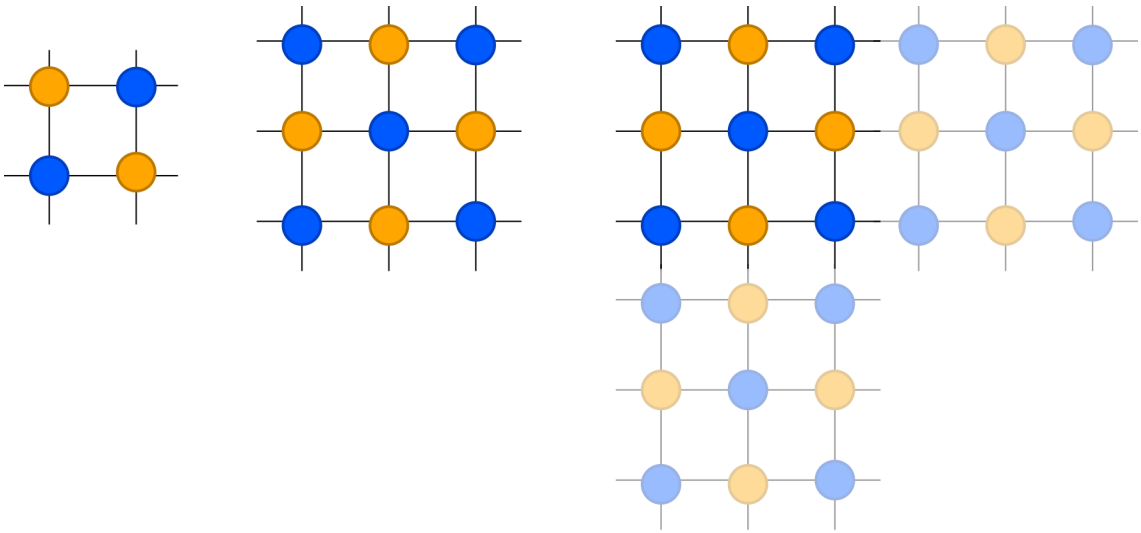

Figure 3.3: An illustration of the importance of sampling cell size. If the symmetry to the left is to be sampled on a 3×3 unit cell (middle), phase boundaries where the symmetry break will be introduced when the periodic boundary conditions are applied (right).

The choice of supercell size for the simulations needs to be handled with care with respect to the ordered phases that might appear. As illustrated in Fig. 3.3, the supercell size should be chosen such that the relevant ordered phases can be resolved

in the cell without phase boundaries. The latter introduce additional interface energy, which means that the energy is not sampled correctly, and ordered phases might be overlooked. It is not trivial how to make this choice, since in principle the ordered phases are not known before sampling. If possible, the supercell selection should be based on a study of the mixing energy of all enumerated structures. In addition, multiple ordered phases might be possible, which further complicates the choice. The approach taken in this thesis work is to start with simulations on a 3×3×3 times the FCC conventional cell for the bulk systems, which yields $4 \cdot 3 \cdot 3 \cdot 3 = 108$ atoms as the FCC conventional cell has 4 atoms. For the surfaces, a 12×12×1 times the prototype cell is used, which yields $10 \cdot 12 \cdot 12 \cdot 1 = 1440$ atoms. Then, additional simulations with other supercells were conducted in some cases, based on prior knowledge of the systems and results from the CE.

Most MC simulations were done with the VCSGC ensemble because of the advantage of being able to sample across multiphase regions. For these simulations, ϕ was varied from -2.2 to 0.2 with a step of 0.02, while κ was kept at 200. In some cases, sampling was done also with the SGC ensemble, since it enables detecting multiphase regions by studying the discontinuities of the free energy derivative as a function of concentration. In these cases, $\Delta\mu$ was varied from -1.5 to $1.5\,\mathrm{eV/atom}$ with a step of 0.01 for the binary systems and 0.02 for the ternary system. The lower resolution for the ternary system is due to the increased number of simulations needed to cover the full ternary system. The canonical ensemble was used in all simulated annealing simulations.

4

Cluster expansion design

This chapter is devoted to presenting insights obtained during this thesis work regarding how to construct, validate, and asses a CE for multicomponent bulk and surface systems.

4.1 Validation of cluster expansions

Before constructing the final CE, it is often useful to construct learning curves to study the influence of parameters, such as the training set size and the number of ECIs, on the CV-RMSE. Based on these studies, one can determine appropriate parameter values and gain intuition on what CV-RMSE values are to be expected, in a more efficient way than studying individual CEs. Examples of such curves are shown in Fig. 4.1, for the AuPd bulk system with reference data produced with an EAM potential. Learning curves are constructed from data obtained during a 5-split, shuffle-split CV. This means that CV is done by fitting the ECIs 5 times, each time the reference data set is split into a training set and a testing set, and the data set is shuffled between the splits meaning that there is no memory of how the previous split was made.

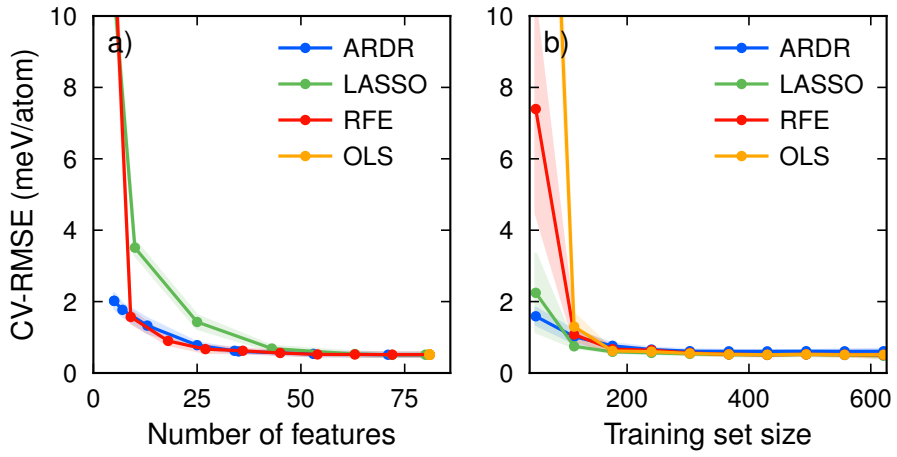

Figure 4.1: Hyperparameter (a) and training set size (b) learning curves for the AuPd bulk system based on reference data calculated with an EAM potential.

Figure 4.1 a) shows what will from now on be referred to as a hyperparameter learning curve, where the hyperparameters of the linear regression methods are varied and the training set size is kept fixed at 90% of the full reference data set. The

hyperparameter of ARDR, LASSO, and RFE controls the sparsity of the solution, which means the number of features (ECIs) that contributes in the fitted model. The less complicated OLS method has no hyperparameter, and as such the number of features is always the number of clusters included in the cluster space. In general, a lower number of features is preferred since it will produce a more efficient model. The hyperparameter learning curve can thus be used to both compare the different methods and find an optimal value of the hyperparameter for the chosen method.

Figure 4.1 b), on the other hand, shows a training set size learning curve where the hyperparameters are fixed while the training set size is varied. The training set size is the number of reference structures, out of the reference data set, used for fitting the model. This curve provides insight in whether the size of the reference data set is appropriate or not. Ideally, one would like to have a training set size learning curve that converges, and the ideal reference data set size would be around the point of convergence.

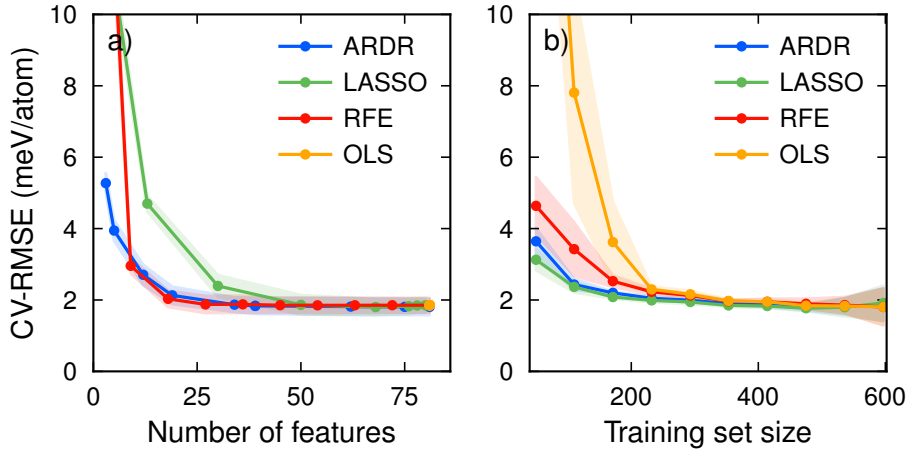

Figure 4.2: Hyperparameter (a) and training set size (b) learning curves for the AuPd bulk system, based on DFT reference data.

Figure 4.2 shows the same learning curves for the AuPd bulk system with DFT based reference data. The CV-RMSE is generally about twice as large as in the case of EAM based data, likely reflecting the more detailed description of the interactions with DFT. The relative performances of the methods are similar to the results for the EAM based reference data. ARDR and RFE are superior when in comes to the number of features versus the CV-RMSE, while ARDR and LASSO performs better in terms of the training set size. Based on this analysis, ARDR is the most suitable method for the problem at hand, and will thus be used in the rest of the thesis work.

Figures 4.3 and 4.4 show the ARDR learning curves for all binary bulk systems and the ternary bulk system, respectively. Based on these results, the hyperparameter for ARDR, λ, is set to 30000. This value is used in all following CEs and training set size learning curves. The training set size learning curves seem to be reasonably converged, meaning that the maximum training set sizes are sufficient.

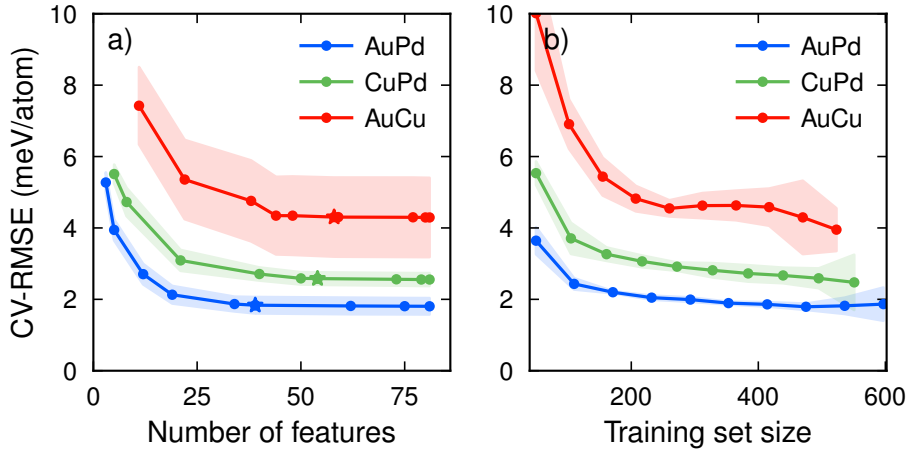

Figure 4.3: Hyperparameter (a) and training set size (b) learning curves for the binary bulk systems, based on DFT reference data and optimized with ARDR. The stars in the hyperparameter curves mark the points where $\lambda = 30000$.

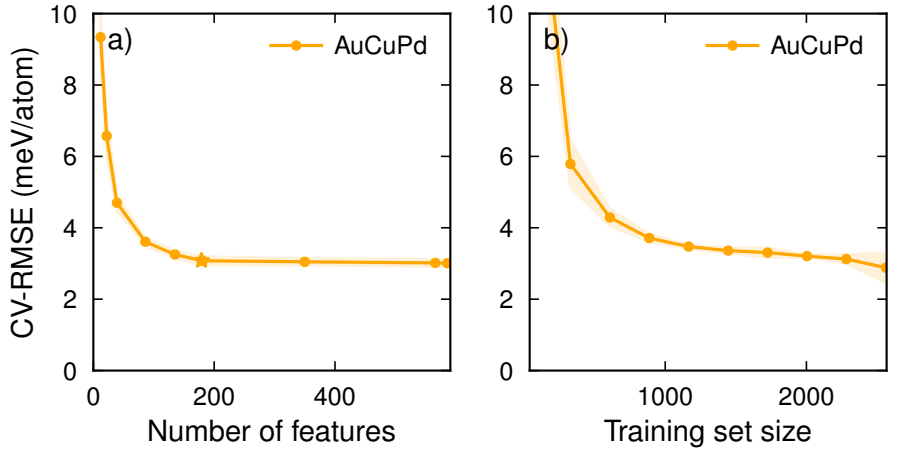

Figure 4.4: Hyperparameter (a) and training set size (b) learning curves for the ternary bulk system, based on DFT reference data and optimized with ARDR. The star in the hyperparameter curve marks the point where $\lambda = 30000$.

4.2 Structure selection for large configuration spaces

Learning curve analysis is useful also for optimizing the structure selection for large configuration spaces, such as for surface CEs.

Figure 4.5 compares two approaches for structure selection, tested out with the EAM potential for the AuPd surface system. Both are based on generation of random configurations on a unit cell with randomly selected dimensions within the range presented in Section 3.1[1]. With the first approach (method 1) the structures

[1]The 3×3 unit cells are not included in any part of this chapter, since they were added later.

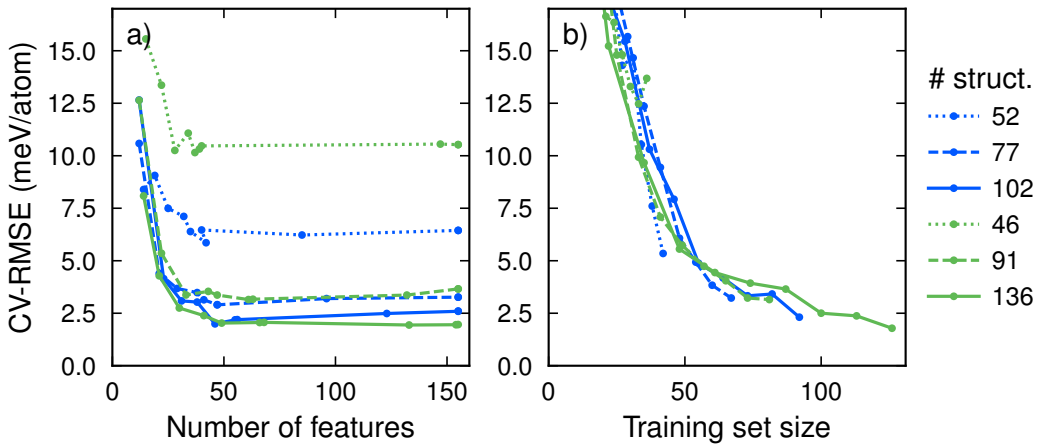

Figure 4.5: Hyperparameter (a) and training set size (b) learning curves for the AuPd system, based on EAM reference data with varying reference data set size. The legend indicates the total number of structures in the reference data set. Method 1 and 2 for structure selection is shown in green and blue, respectively.

are uniformly distributed over the concentration range while with the second approach (method 2) the structures are distributed in a stair-like fashion such that the number of structures peaks around 50 %. Both methods perform reasonably well in comparison to the bulk studies, but method 2 is more efficient as it requires fewer reference structures.

With that being said, one should be careful when comparing CV-RMSE scores based on different structure selection methods. While the score reflects the performance of the method, it also reflects the homogeneity of the reference data set. If the reference data set contains similar structures, the training and testing sets will be correlated and the CV-RMSE will be lower. In this case, the choice of method 2 can be further motivated by the fact that there is a larger number of available configurations at concentrations around 50 %, meaning that this approach gives a better sampling of the entire configuration space.

A third approach tested (method 3) was to set up the set of reference structures in the same manner as in method 2, followed by an optimization of the condition number of the sensing matrix. This included MC simulated annealing where the structures were randomly swapped out within the same concentration, while using the condition number as the thermodynamic potential to be minimized during simulation. This approach yields a reference data set that is optimized in the sense that the rows of the corresponding matrix equation will be as uncorrelated as possible. A comparison between methods 2 and 3 is shown in Fig. 4.6. The difference between these two approaches is not significant enough to motivate the extra effort required to optimize the data set. However, this method might be worth revisiting for larger reference data set sizes where the random configurations might be more correlated.

Based on these results, method 2 was chosen for surface reference structure selection. Learning curves for the binary surfaces with DFT based reference data are shown in Fig. 4.7. The training set size learning curves are not converged but rather suggest a linear dependence between the training set size and the CV-RMSE,

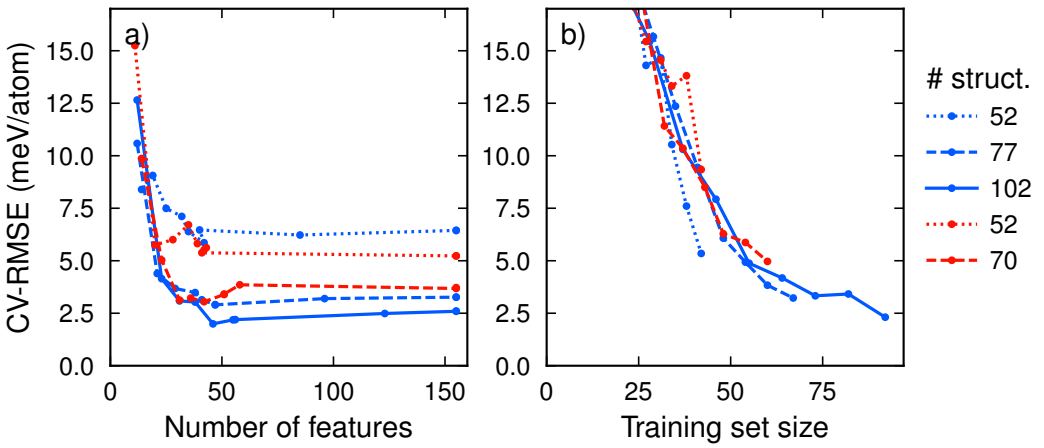

Figure 4.6: Hyperparameter (a) and training set size (b) learning curves for the AuPd system, based on EAM reference data. The reference data sets are chosen such that the number of structures is peaked around 50 % concentration and the legend indicates the total number of structures in the set. Method 2 and 3 is shown in blue and red, respectively.

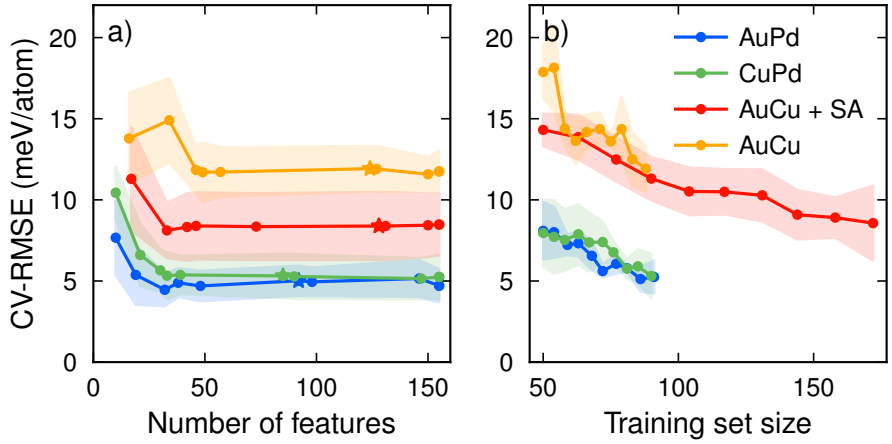

Figure 4.7: Hyperparameter (a) and training set size (b) learning curves for the binary surface systems, based on DFT reference data and optimized with ARDR. The stars in the hyperparameter curves mark the points where $\lambda = 30000$. For the AuCu system, the results both before (orange) and after (red) simulated annealing are shown.

indicating that a larger reference data set would improve the CE. Simulated annealing can be used during surface selection also to expand an existing reference data set. This is done to improve the high CV-RMSE for the AuCu surface system. By constructing a CE based on the existing reference data set and performing regular simulated annealing, low energy structures structures can be generated and added to the reference data set. In contrast to the previous simulation annealing to optimize the condition number, this approach will likely produce correlated structures and thus worsen the condition number. On the other hand, low energy structures are more likely to appear in a real system, and one can thus argue that a reference

data set with low energy structures better represents reality.

To conclude this section, structure selection of large configuration spaces is a complicated issue. The aspects to keep in mind are i) how well the configuration space is sampled, ii) how well the structures represents the reality and iii) the correlation between structures (and thus the condition number of the sensing matrix). It is not always possible to optimize the surface selection with respects to all aspects, and the approach taken might depend on the problem at hand.

4.3 Cluster expansions vs. EAM potential

Even if CEs are first-principle based, there will always be an error when comparing a CE prediction with the corresponding DFT calculation. While the size of this error is a relevant measurable, it is also important to keep in mind that usually, it is not feasible to perform ground state searches and MC simulations on multicomponent systems with DFT calculations alone, due to the extremely large configuration space. It is therefore meaningful to also compare CEs to other methods that could be used interchangeably, such as EAM potential calculations, to get a better understanding of the usefulness of a CE.

Figure 4.8 shows CE predictions and EAM calculations of mixing energies, compared to the DFT calculated values that are regarded as the true mixing energies. The CEs are produced during a 5-split validation, as in Section 4.1, such that 5 independent CEs are obtained. In every split, ten reference structures are used for testing. The mixing energies of all testing structures are calculated using both the corresponding CE and an EAM potential. In this way, the CE used in a prediction is independent of the structure in question, which enables a more fair comparison than if the structure had been involved in training.

This comparison is done for bulk and surface systems in Fig. 4.8. In both cases, it is clear that the CEs outperform the EAM potentials, even in the case of the AuCu-surface where the CV-RMSE scores seemed alarmingly large in Section 4.2.

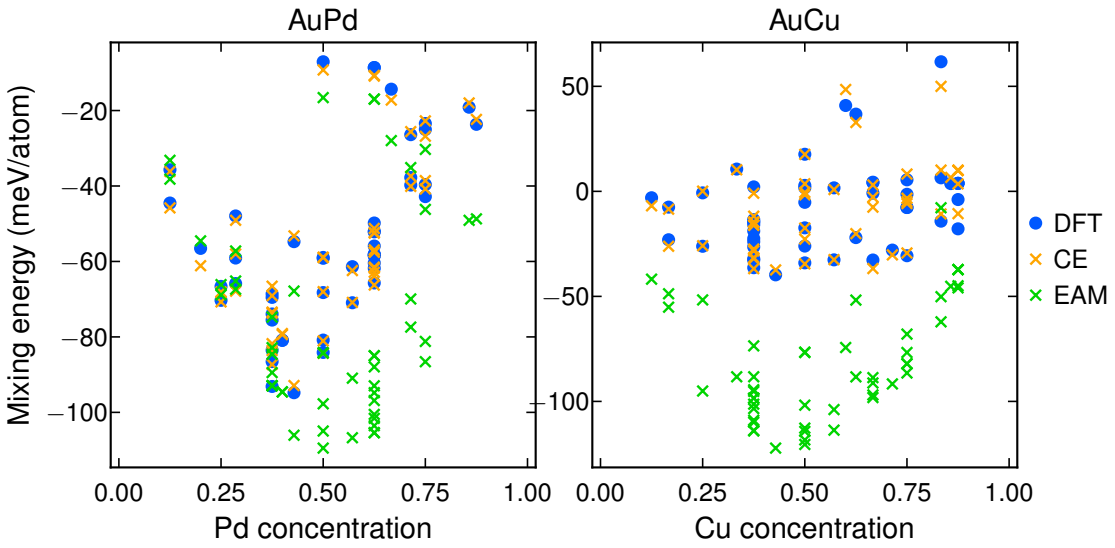

(a) Bulk

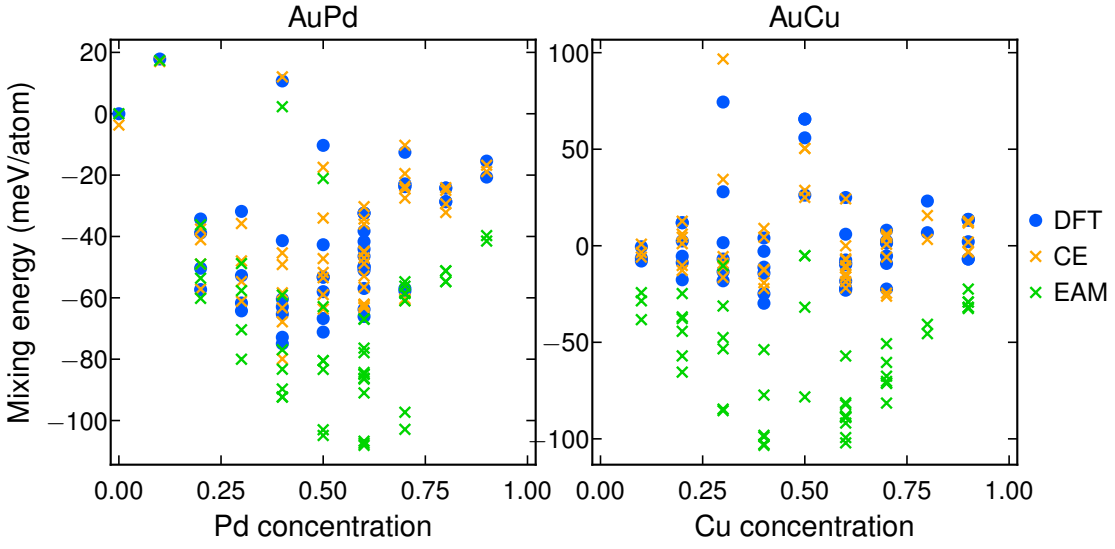

(b) Surfaces

Figure 4.8: A comparison between calculating the mixing energy with CEs and with an EAM potential, for the bulk and surface AuPd and AuCu systems.

5
Bulk

In this chapter, the results of CE construction and sampling for the bulk systems are presented and discussed.

5.1 Cluster expansions

System	CV-RMSE	RMSE	#structures	#orbits	#features	ΔE
AuPd	1.9	1.7	607	81	41	97
AuCu	4.6	3.8	533	81	79	131
CuPd	2.7	2.3	561	81	55	114
AuCuPd	3.8	2.8	2573	586	189	209

Table 5.1: Characteristics of final bulk CEs. RMSE and ΔE are given in units of meV/atom. The difference between CV-RMSE and RMSE is that CV-RMSE is calculated during validation from the structures not included in the training data set, while RMSE is calculated against all reference structures after training the final CE. The total number of structures in the reference data set is #structures, the number of orbits in the cluster space is #orbits, the number of non-zero ECIs in the final CE is #features and the difference between the maximum and minimum mixing energy in the reference data set is ΔE.

The characteristics of the CEs constructed are presented in Table 5.1. Overall, the CV-RMSE scores agree well with the learning curves presented in Section 4.1, with slightly lower values since the CEs are properly trained with the full reference data set. Table 5.1 also presents the total energy span of the reference data, which puts the CV-RMSE scores in context. All CV-RMSE scores are within 1.8-3.5% of the corresponding energy interval.

Figure 5.1 a) shows the mixing energies of the reference structures over the concentration range of the binary systems, both calculated with DFT and predicted with CEs. The AuPd and CuPd system have similar mixing energy graphs, with a deep minimum and almost all data points on the negative side. The AuCu system, on the other hand, have a shallower minimum and many reference structures have positive mixing energy, suggesting a less stable mixing. Figure 5.1 b) shows how the predicted mixing energy deviates from the target mixing energy, for the reference structures. The higher CV-RMSE for the AuCu system manifests as a larger deviation of predicted energy compared to the other systems, especially for high energy

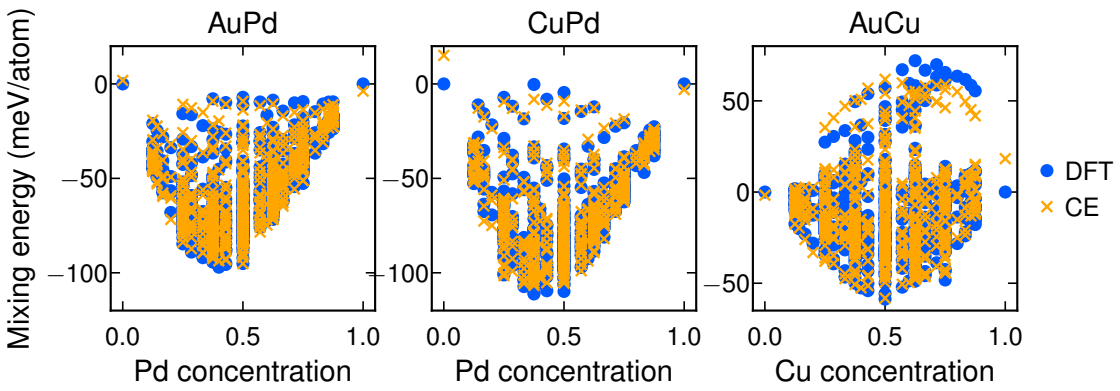

(a) The mixing energies of the reference structures, calculated with DFT and predicted with CEs.

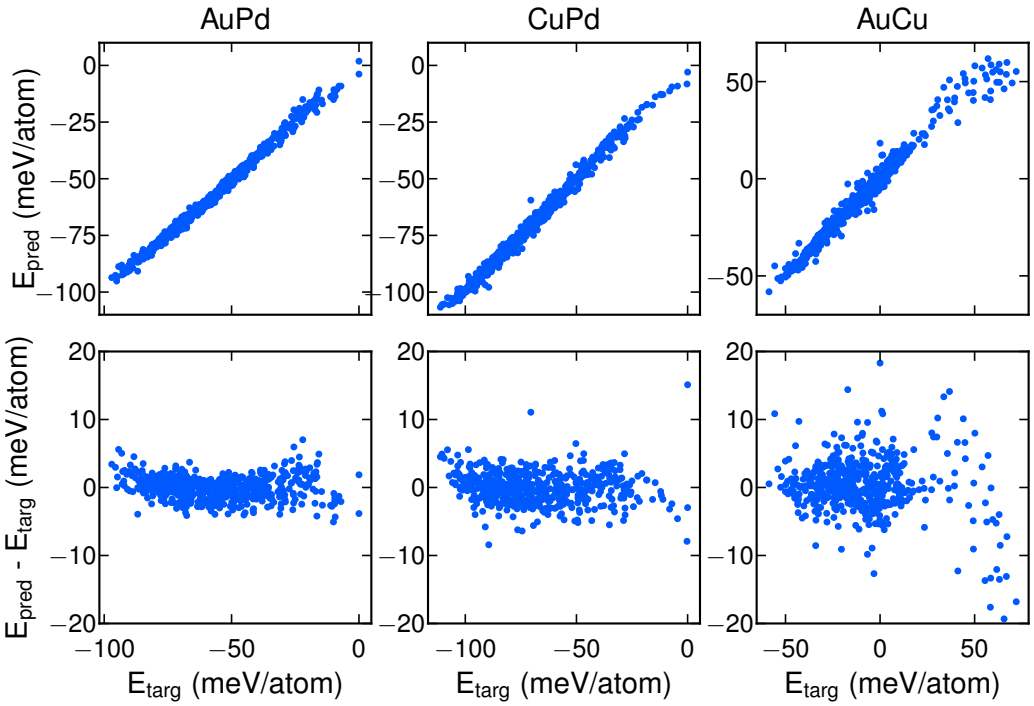

(b) The predicted mixing energies plotted against the target energies.

Figure 5.1: Comparisons of the target mixing energies (calculated with DFT) and the corresponding CE predictions of the bulk binary systems.

structures.

Figure 5.2 shows a comparison of the DFT calculated and CE predicted values of the mixing energies for all reference structures used to construct the ternary CE. These plots are similar to the corresponding plots for the binary systems, in Fig. 5.1, indicating that the accuracy is preserved when introducing a third element. The minimum mixing energies of all ternary and binary structures with less than ten atoms in the unit cell is shown in Fig. 5.3, calculated with the ternary CE.

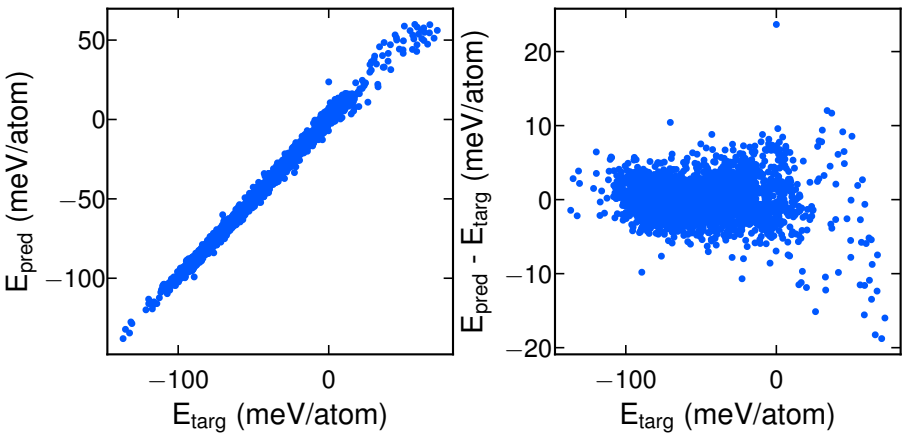

Figure 5.2: Comparison of the target mixing energies (calculated with DFT) and the corresponding CE predictions for the bulk ternary system.

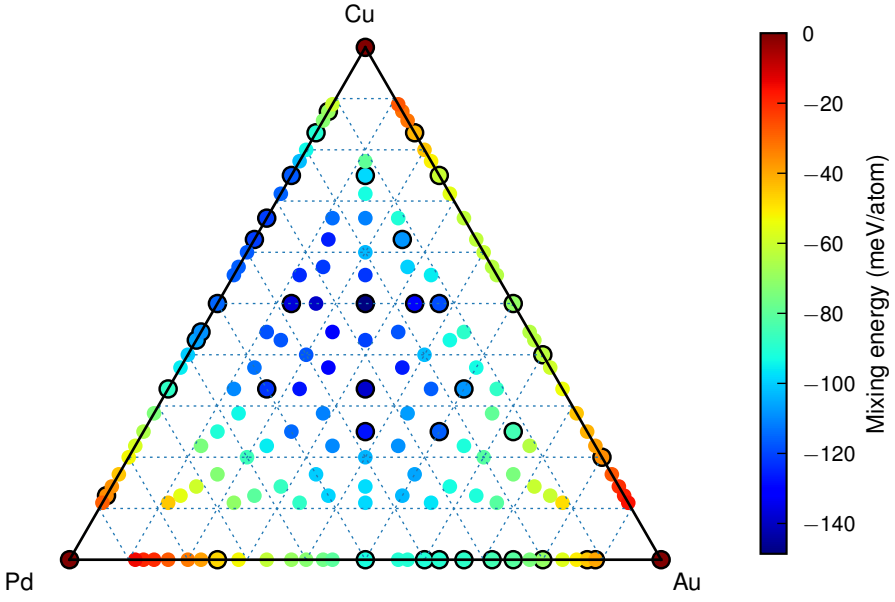

Figure 5.3: The minimum mixing energy of all ternary structures with less than ten atoms in the unit cell, calculated with the ternary CE. The convex hull structures are marked with black edges.

5.2 Monte Carlo sampling of the binary systems

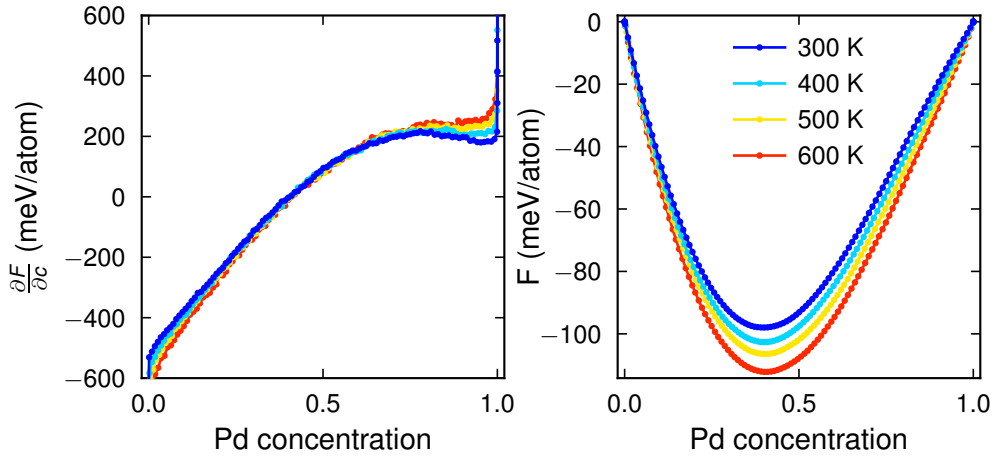

(a) AuPd

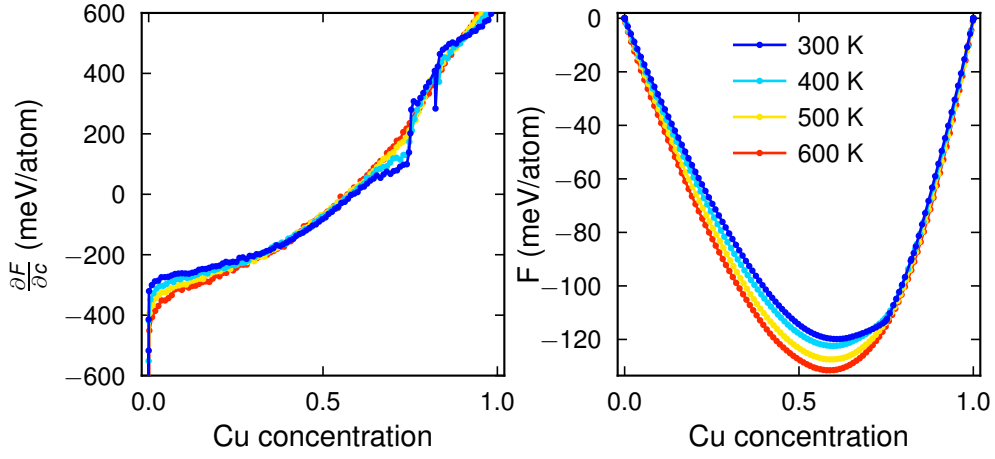

(b) CuPd

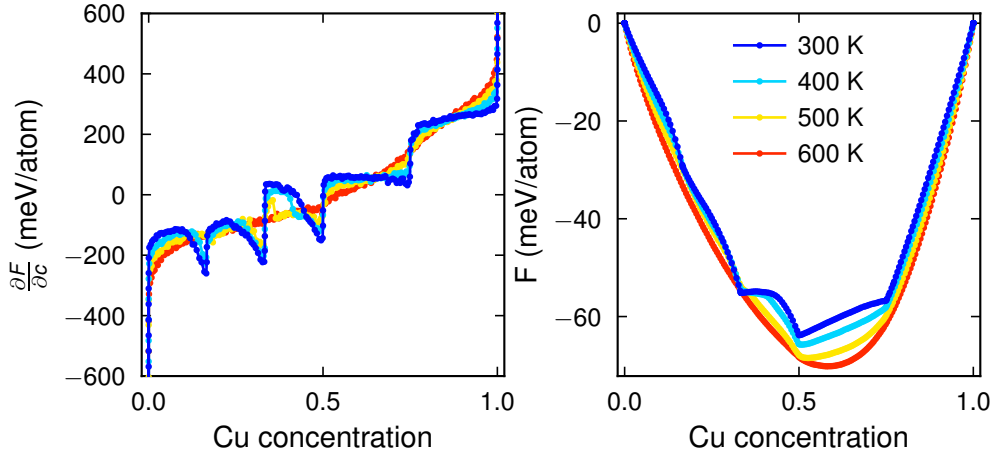

(c) AuCu

Figure 5.4: The free energy derivative and free energy of the binary bulk systems, obtained by MC sampling (50000 trial steps, 3×3×3 supercell) in the VCSGC ensemble at different temperatures.

The free energy derivative and free energy curves for the binary systems, obtained by MC sampling, are shown in Fig. 5.4. The sampling of the AuPd system, Fig. 5.4 a), results in a smooth free energy derivative curve and a concave up free energy curve, indicating complete miscibility at all concentrations. For the CuPd system, in Fig. 5.4 b), the free energy derivative has some jumps, but the free energy curve is still concave up at all temperatures. This indicates that there is a phase at around 0.75% Cu low in energy, but not low enough to cause phase separation. It should be noted that other work suggest the presence of a BCC ordered phase in the CuPd system [38], which cannot be found with the present method since the CE is limited to FCC structures. The sampling of the AuCu system in Fig. 5.4 c), on the other hand, shows several jumps in free energy derivative and convex up regions in the free energy curve. These results indicate a phase diagram with multiple ordered phases, which is analysed further in the following section.

5.2.1 Ordering in the bulk AuCu system

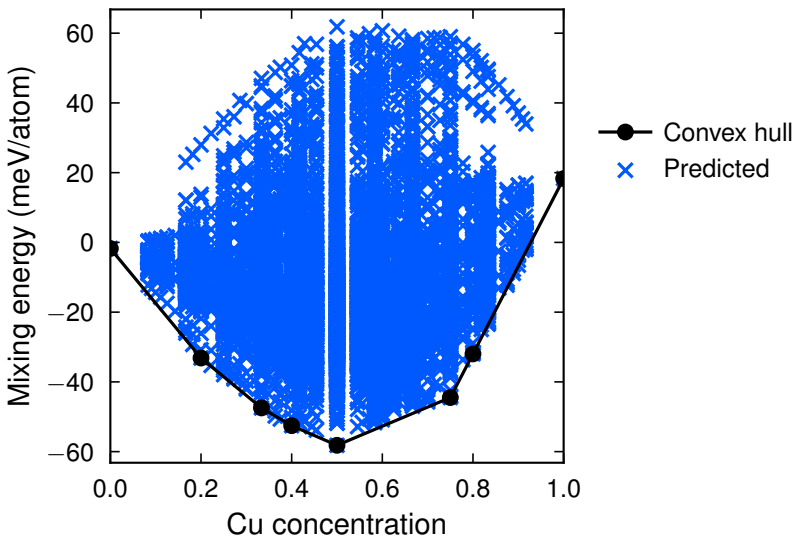

Figure 5.5: CE predicted mixing energies for all AuCu structures with less than 13 atoms in the unit cell. The structures on the convex hull are represented by black circles.

To construct a phase diagram for AuCu, more detailed sampling is necessary. Figure 5.4 shows the CE predicted mixing energies of all AuCu structures with less than 13 atoms in the unit cell. The structures on the convex hull represents candidate ordered phases and the MC supercell should ideally be able to resolve all of these structures without phase boundaries. By comparing the unit cells of the convex hull structures with different supercells, it is found that a 15×3×3 times the FCC conventional cell is cell suitable.

Sampling of the free energy derivative of the AuCu system in the SGC ensemble, compared with the VCSGC sampling from Fig. 5.4 c), is shown in Figure 5.6. Multi-phase regions are revealed by gaps in the SGC curve and jumps in the VCSGC curve. Based on these results, a phase diagram can be sketched, as in Fig. 5.7 e).

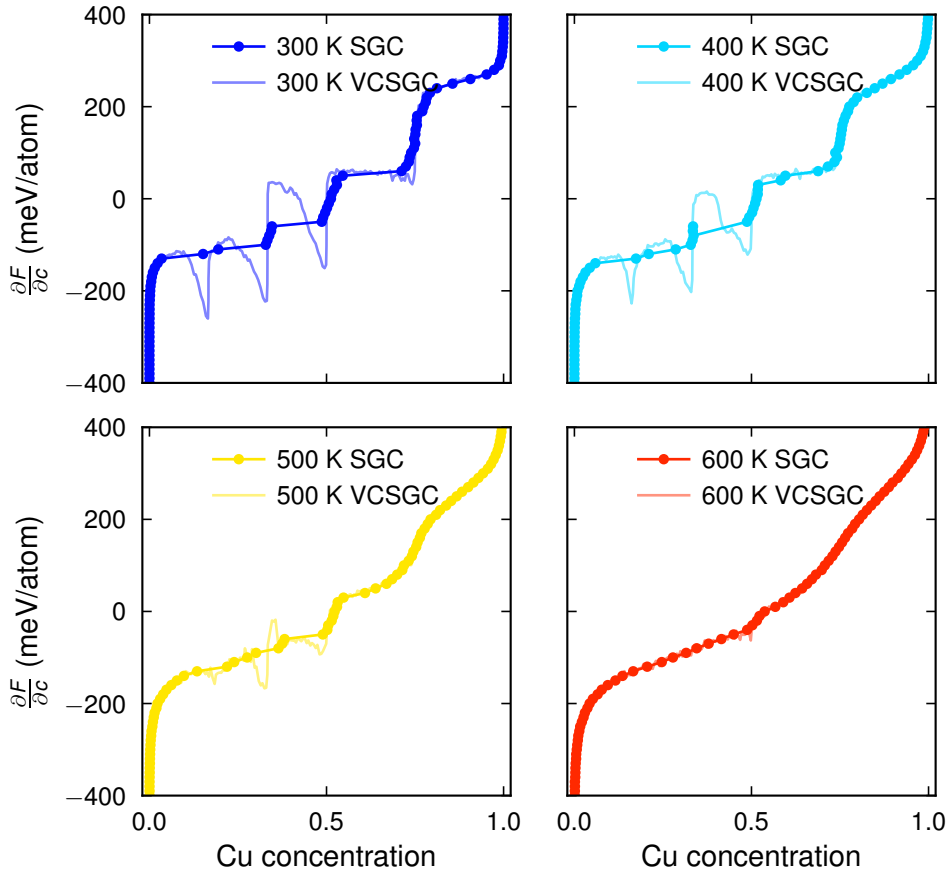

Figure 5.6: The free energy derivative of AuCu, obtained by MC sampling in the VCSGC and SGC ensembles at different temperatures. The VCSGC sampling is done with 50000 trial steps and a 3×3×3 supercell. The SGC sampling is done with 150000 trial steps and a 15×3×3 supercell.

The corresponding ordered phases are illustrated in Fig. 5.7 a-e). This step could obviously be done more carefully, with higher resolution in both temperature and concentration, to obtain a more accurate phase diagram. For the purpose of this thesis, the aim is to get a qualitative understanding of the ordered phases rather than a reliable phase diagram.

5.3 Monte Carlo sampling of the ternary system

The mixing energy obtained by MC sampling of the ternary system is shown in Fig. 5.3. Recall that the step size of $\Delta\mu_i$ is doubled compared to the SGC sampling of binary systems, which makes it harder to distinguish multiphase regions from gaps in resolution. It is, however, clear that as the temperature decreases, the plot becomes more sparse indicating that phase separation do appear.

At all temperatures, an ordered phase around the $AuCu_2Pd$ composition is present, extending towards the AuCu axis with constant Cu concentration at 50 %. A similar feature appears slightly below at 33 % Cu. These phases should be further inves-

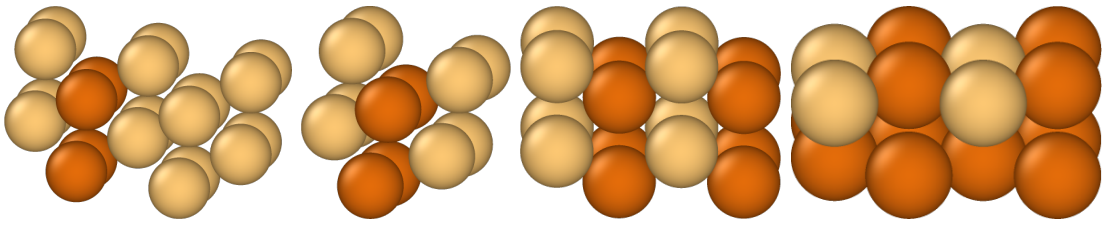

(a) Au_4Cu (b) Au_2Cu (c) AuCu (d) $AuCu_3$

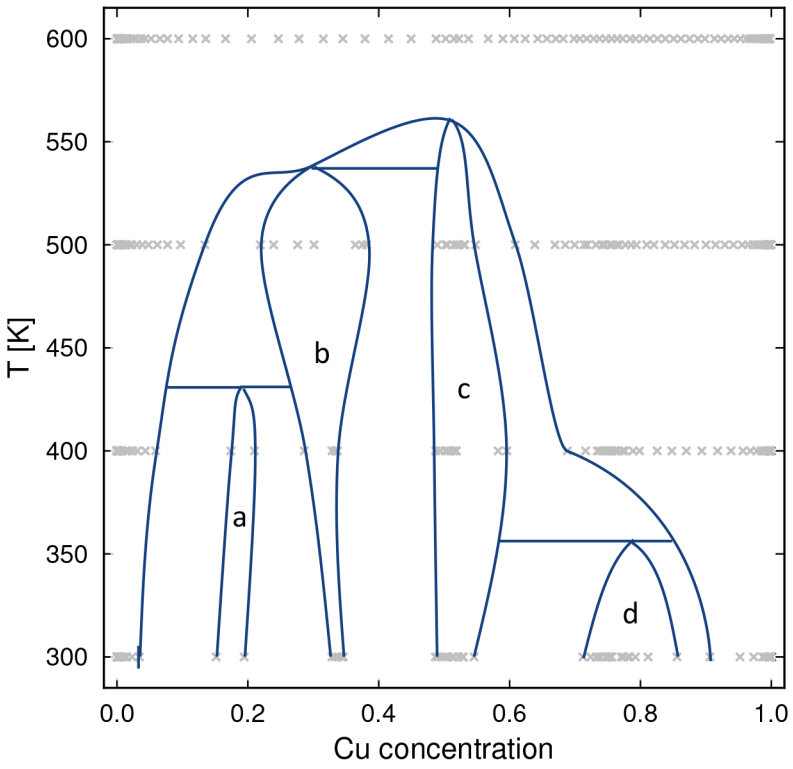

(e) Phase diagram

Figure 5.7: A sketch of the AuCu phase diagram (e) and the corresponding ordered phases (a-d). The grey crosses are the concentrations from the SGC sampling in Fig. 5.6, acting as a guide for the phase diagram.

tigated with respect to the competing ordered BCC CuPd phase. The gaps at the AuPd axis on the Pd rich side are surprising given that the bulk results indicate complete miscibility. The gap position is, however, inconsistent with temperature decrease, indicating that this is not a real phase separation but rather a resolution issue.

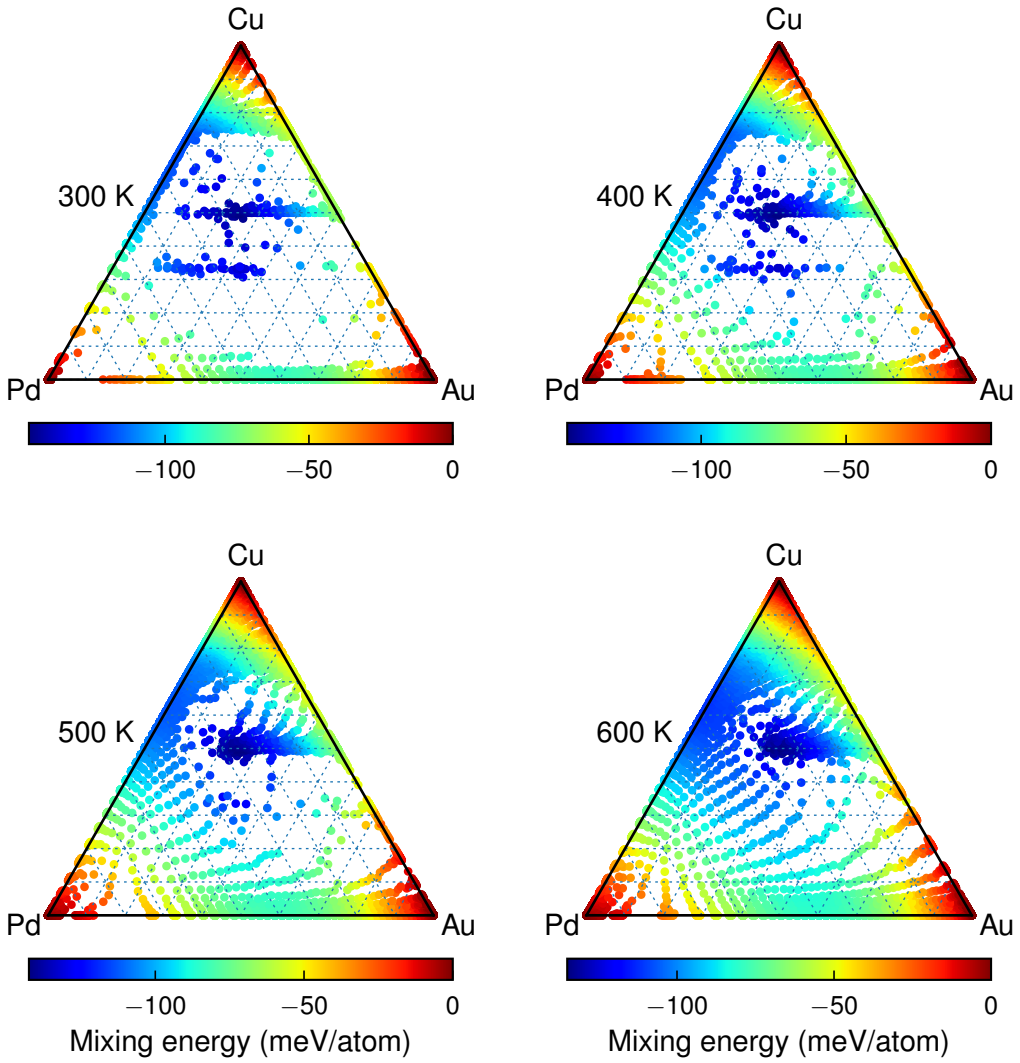

Figure 5.8: The mixing energy of the ternary bulk systems, obtained by MC sampling (50000 trial steps, 3×3×3 supercell) in the SGC ensemble at different temperatures.

6
Surfaces

In this chapter, the results of CE construction and sampling for the surface systems are presented and discussed.

6.1 Cluster expansions

System	CV-RMSE	RMSE	#structures	#orbits	#features	ΔE
AuPd	6.6	1.5	110	155	86	95
AuCu	10.6	4.0	188	155	124	126
CuPd	6.9	1.9	110	155	98	98

Table 6.1: Characteristics of final surface CEs. RMSE and ΔE are given in units of meV/atom. The difference between CV-RMSE and RMSE is that the CV-RMSE is calculated during validation from the structures not included in the training data set, while the RMSE is calculated against all reference structures after training the final CE. The total number of structures in the reference data set is #structures, the number of orbits in the cluster space is #orbits, the number of non-zero ECIs in the final CE is #features and the difference between the maximum and minimum mixing energy in the reference data set is ΔE.

The CE characteristics are presented in Table 6.1. The CV-RMSE scores are in line with the learning curves, and as expected they are significantly larger than for the bulk systems. Compared the total energy spans, the CV-RMSE scores constitute 6.9-8.4%. Surfaces are generally more complicated to model and in addition, the number of reference structures are lower than for the bulk systems. Another difference compared to the bulk CEs is that the RMSE is significantly lower than the CV-RMSE. It is expected that the RMSE is lower than the CV-RMSE, since the RMSE is calculated after training the model against the full data set. If the difference is large, however, it implies that the numerical fitting of ECIs performs well, but that the physics is not picked up properly since the error for structures excluded from training is high.

The mixing energies of the reference structures, calculated with DFT and predicted with CEs, are shown in Fig. 6.1. The energy curves over the concentration ranges, in Fig. 6.1 a) are similar to the bulk results with deep minima for the AuPd and CuPd systems and shallower minimum for the AuCu systems with even more

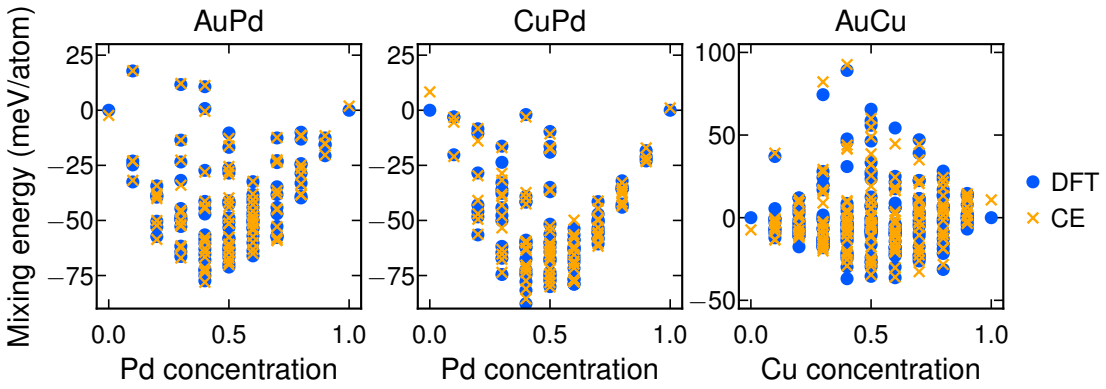

(a) The mixing energies of the reference structures, calculated with DFT and predicted with CEs.

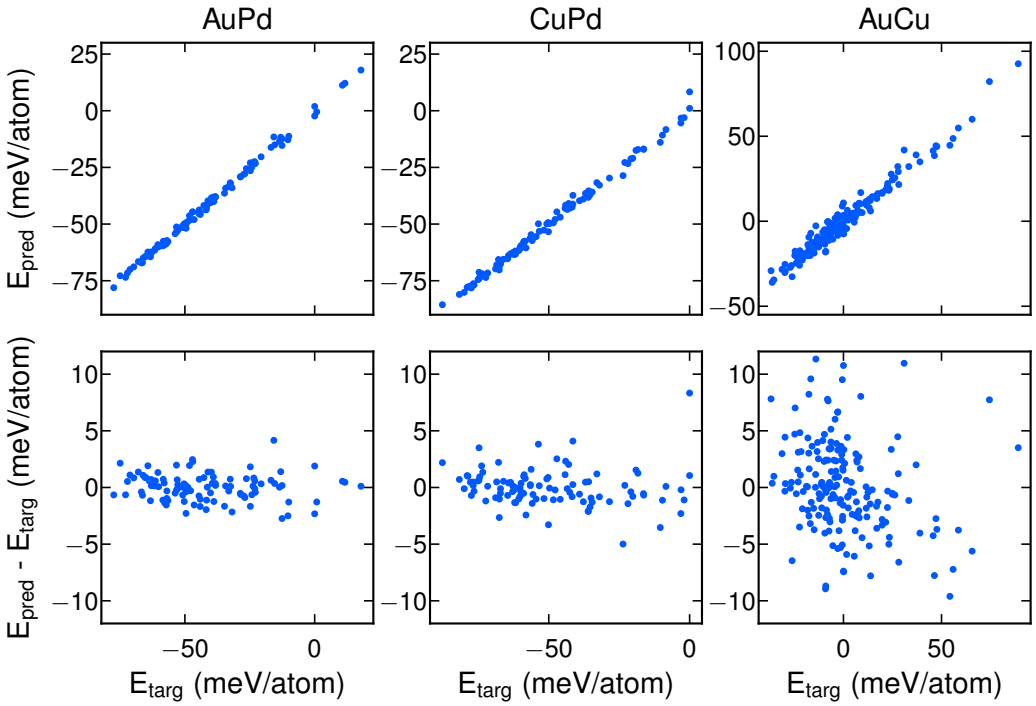

(b) The predicted mixing energies plotted against the target energies.

Figure 6.1: Comparisons of the target mixing energies (calculated with DFT) and the corresponding CE predictions of the binary surfaces.

structures in the positive side. The comparison between the predicted and target energies in Fig. 6.1 b) shows a linear relation between the two.

6.2 Monte Carlo sampling of binary surfaces

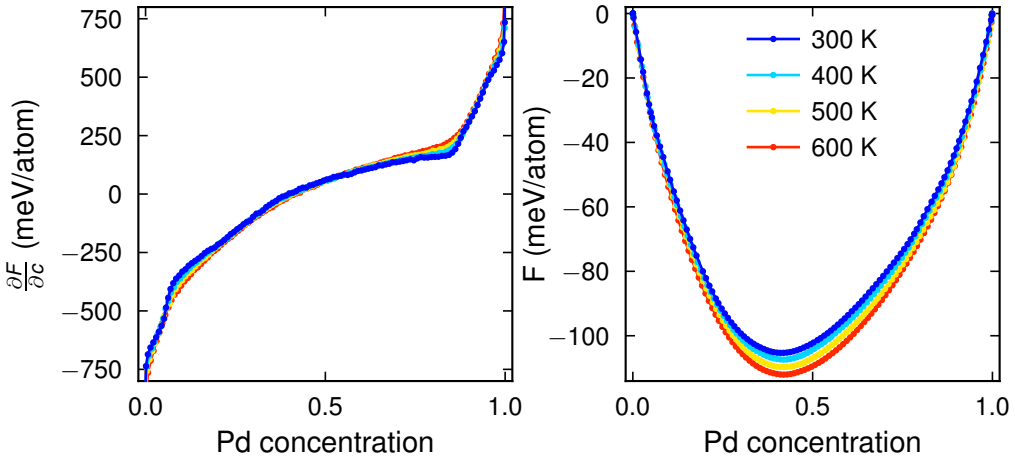

(a) AuPd

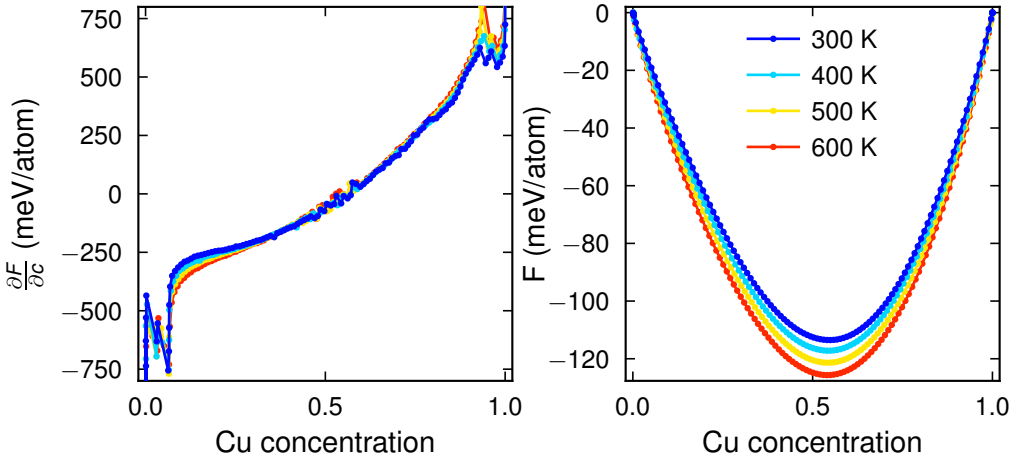

(b) CuPd

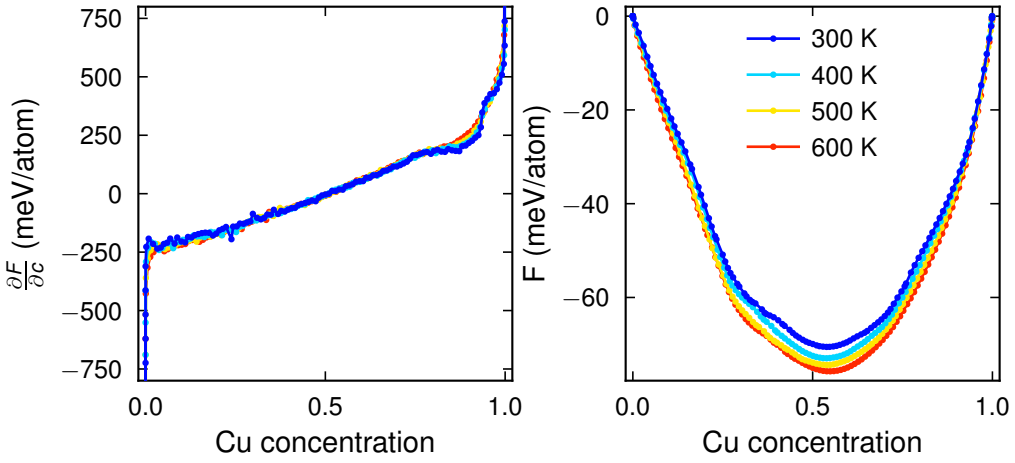

(c) AuCu

Figure 6.2: The free energy derivative and free energy of the binary surfaces, obtained by MC sampling (50000 trial steps, 12×12×10 supercell) in the VCSGC ensemble at different temperatures.

The free energy derivative and free energy obtained from MC sampling are shown in Fig. 6.2. The free energy curves of the surface systems have similar general features as in bulk, but some features, such as the AuCu ordering, are less pronounced. MC sampling of surface slabs is different from bulk, since the ordering is more complex. Bulk ordering might be present in the inner layer as well as ordering at the surfaces and between the surface layers (i.e. surface segregation). By simply studying the free energy curve, it is not possible to distinguish between these competing effects.

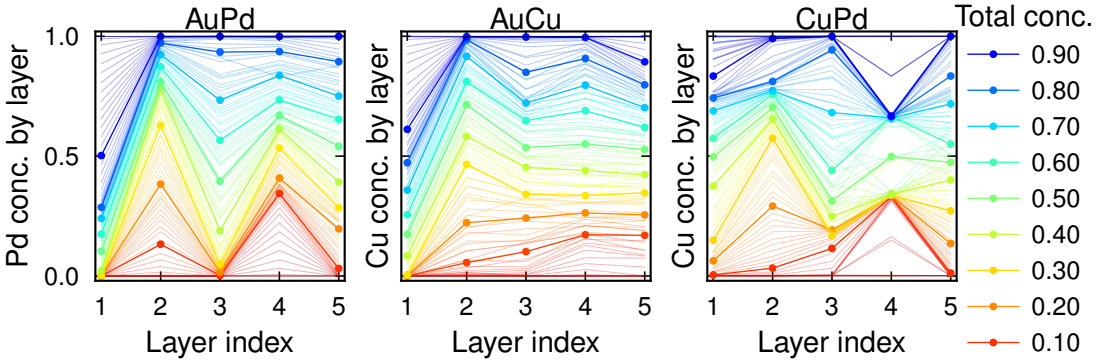

Figure 6.3: The average composition per layer calculated from the MC simulation (50000 trial steps, 12×12×10 supercell). The matching layers on each side of the slab have been averaged such that layer index one represent layer one and ten, and so forth. The color indicates the overall concentration of the supercell, and the y-axis the concentration by layer.

To study the surface segregation, the average concentration of each layer can be extracted from the MC simulation, as in Fig. 6.3. Starting with the AuPd system, this graph shows a pronounced surplus of Au at the surface. In addition, an interesting segregation mechanism, where the concentration oscillates between the layers, is revealed. The surplus of Au at the surface is followed by a deficit of Au in the second layer, followed by another surplus of Au in the third layer, and so on. This behaviour is strong for Au-rich simulations, continuing into layer five, indicating that ten layer slabs are not sufficient to obtain bulk conditions in the middle. The AuCu system also show a strong tendency for Au to segregate towards the surface. Cu-rich simulations show a similar, but less pronounced, oscillation pattern. The concentration by layer is reasonably converged at the fifth layer, indicating that ten layer slabs are sufficient to include bulk conditions in the AuCu system. The CuPd system shows only a small surplus of a few percent of Pd at the surface. The concentration of the inner layers, on the other hand, show extreme oscillations. The effect at the fourth layer is particularly striking, where the majority of the simulations have Cu concentration at 33 or 66 %.

The oscillation of concentration between the layers is an important result, highlighting the importance of computational studies. Experimental studies might not disclose this feature, since it is often challenging to probe the first layer only. If the measured segregation is averaged over a few layers, the effect would be underestimated in the present cases. Other EAM based work [39] have found similar behaviour for the AuPd system. The general segregation tendencies at the surface

are also confirmed by other work [40, 41].

To further investigate the segregation and ordering between layers, the same results are visualized again by plotting the concentration of each layer against the total concentration in Fig. 6.4, 6.5 and 6.6. The offset from the diagonal displays the surplus or deficit of atoms and ordered phases will appear as steps. Here, results at 100 K are included to highlight ordering effects. The surface ordering can also be assessed by visually studying the atomic configuration of the surface slabs after MC simulation. A few snapshots are selected to represent the observed ordering patterns.

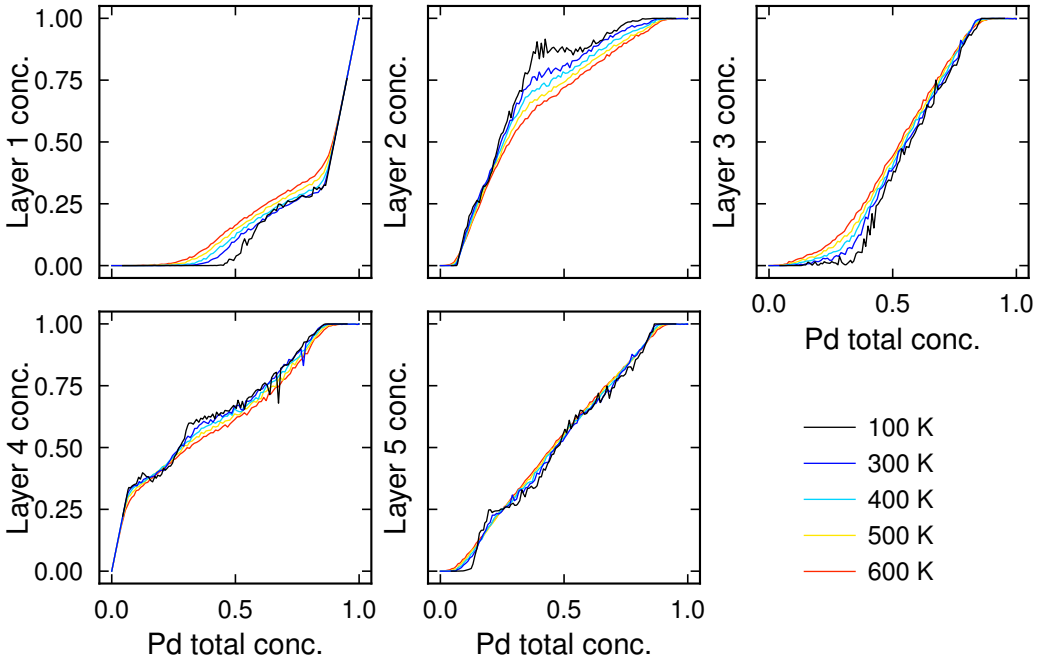

(a) The average composition per layer compared to the total concentration for the AuPd system, calculated from the MC simulation (50000 trial steps, 12×12×10 supercell), at different temperatures.

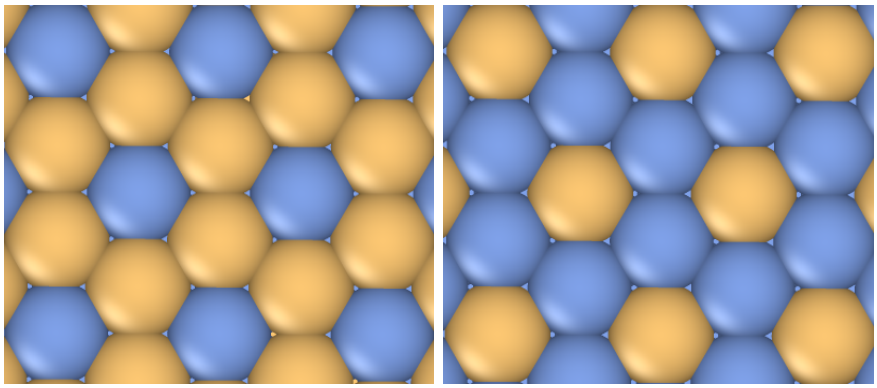

(b) Au_2Pd (c) $AuPd_2$

Figure 6.4: The concentration by layer (a) of the AuPd surface system and identified atomic configurations at the surface (b)-(c) after MC simulation at 300 K.

Figure 6.4 a) shows the concentration of each layer compared to the total concen-

tration for the AuPd system. At the surface layer, a noticeable step appears at 33 % Pd surface concentration. This step corresponds to the ordering observed in Fig. 6.4 b). By studying the atomic configurations at higher Pd-concentration, the reversed ordering pattern in Fig. 6.4 c) is also found. This does not appear as a step in the concentration graph, which is probably due to the fact that Pd tends to avoid the surface. The concentration graphs for the inner layers show the oscillation behaviour between the layers. In addition, steps can be distinguished at 66, 33 (layer 4) and 25 (layer 5) % Pd, indicating some surprising ordering phenomena. Since the surface segregation profile in Fig. 6.3 indicates that the slabs are too thin to simulate bulk behaviour, no reliable comparison to the bulk results can be made.

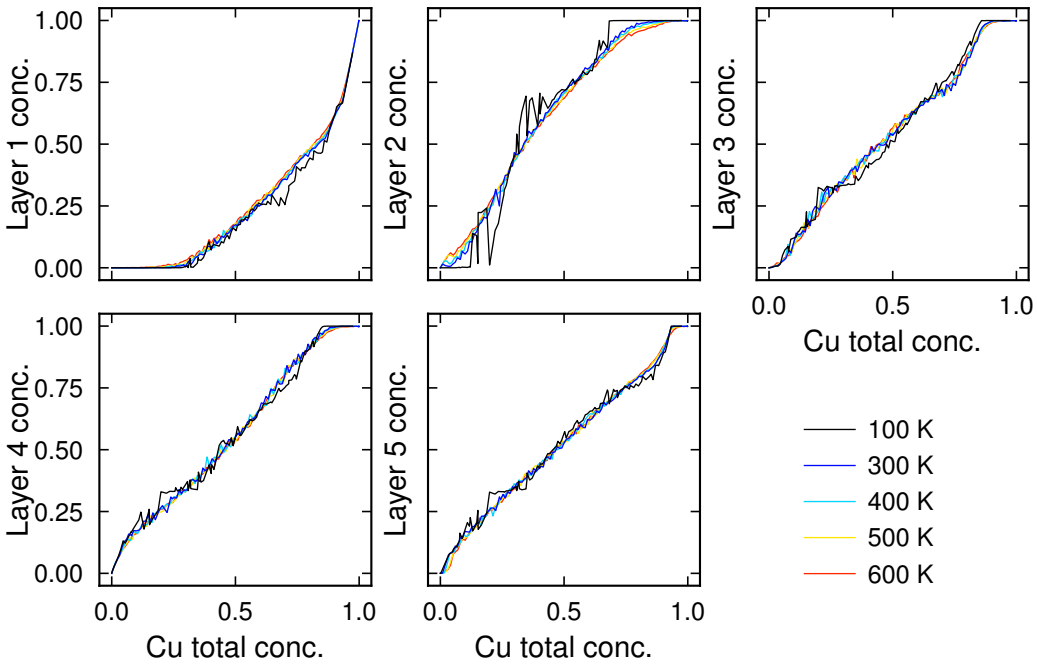

(a) The average composition per layer compare to the total concentration for the AuCu system, calculated from the MC simulation (50000 trial steps, 12×12×10 supercell), at different temperatures.

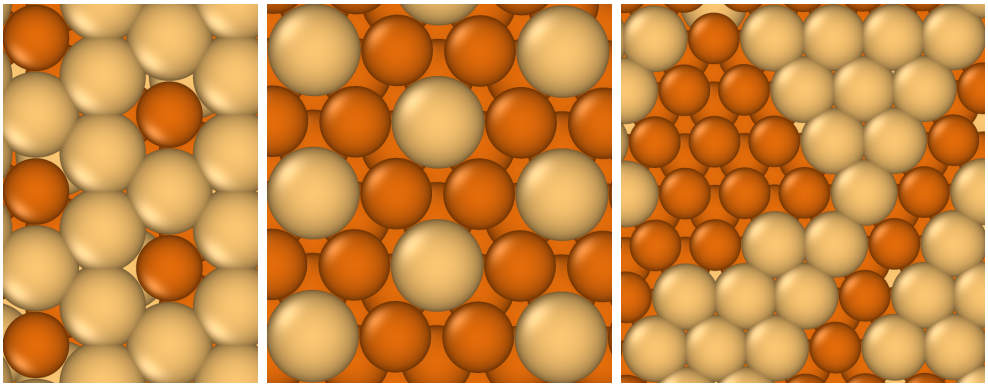

(b) Au_3Cu (c) $AuCu_2$ (d) Clustering

Figure 6.5: The concentration by layer (a) of the AuCu surface system and identified atomic configurations at the surface (b)-(d) after MC simulation at 300 K.

The concentration of each layer compared to the total concentration for AuCu is shown in Fig. 6.5 a). Here, the surface layer has a step at 25 % Cu and a barely noticeable kink at 66 % Cu. For the most part, the atomic configurations at the surface at 300 K forms clusters, as in Fig. 6.5 d), rather than ordered phases, which is reflected by the lack of steps in the 300 K curve. Ordered patterns corresponding to 25 and 66 % Cu are, however, observed on some surface areas, as visualized in Fig. 6.5 b-c). In the inner layers, steps can be distinguished at 33 and 75 % Cu. This ties back to the bulk results where Au_2Cu and $AuCu_3$, among others, are identified as ordered phases of the bulk.

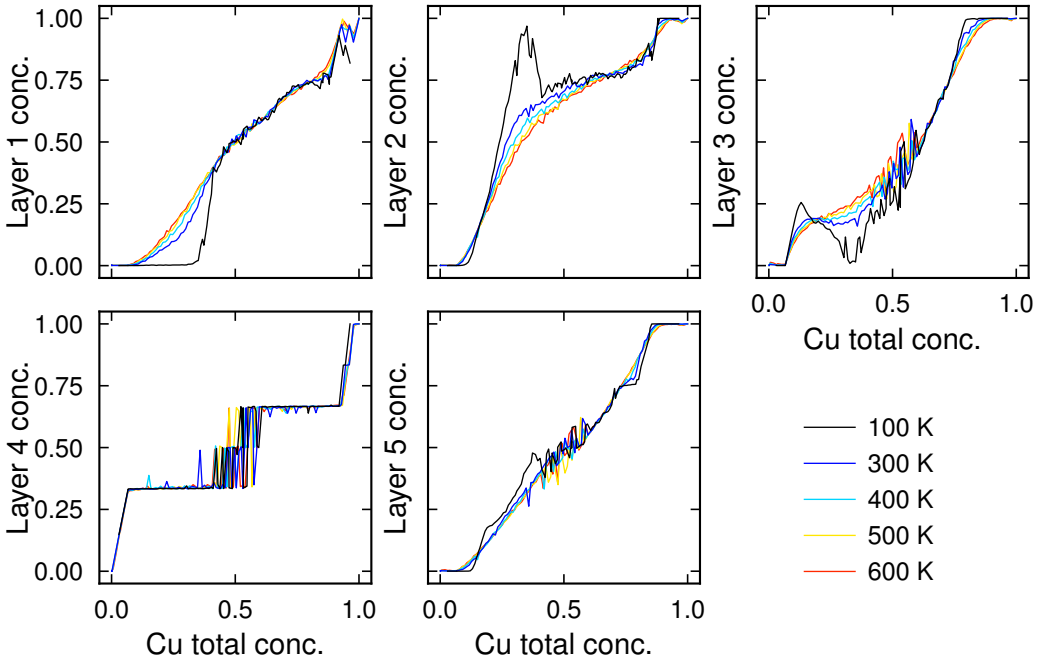

(a) The average composition per layer compare to the total concentration for the CuPd system, calculated from the MC simulation (50000 trial steps, 12×12×10 supercell), at different temperatures.

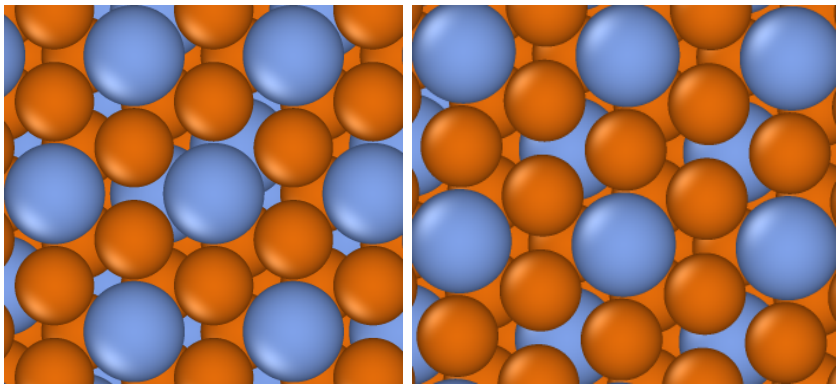

(b) Cu_2Pd (c) Cu_3Pd

Figure 6.6: The concentration by layer (a) of the CuPd surface system and identified atomic configurations at the surface (b)-(c) after MC simulation at 300 K.

For the CuPd system, the concentration of each layer compared to the total con-

centration is shown in figure Fig. 6.6 a). In the surface layer, steps appear at 66 and 75 % Cu, while there is no apparent ordering in the Pd-rich region. The corresponding patterns can be found in the atomic configurations, as shown in Fig. 6.6 b-c). A very striking feature of Fig. 6.6 a) is the extreme ordering of the fourth layer, also visible in Fig. 6.3. There are pronounced steps at 33 and 66 % Cu, and a slightly less pronounced steps at 50 % Cu. This feature is unexpected and it is not certain if this is a real effect or due some error, such as nonphysical ECIs in the CE or strain imposed due to insufficient thickness of the slabs. Further investigation is thus needed.

7
Conclusion

This thesis outlines the importance and performance of CEs in studies of multi-component systems, such as the AuCuPd system. It is found that with a relatively small number of reference calculations, a CE can be trained to predict the energies in a complex configuration space, with accuracy far exceeding EAM potentials. This shows the potential of using CEs to benefit from ab initio calculations on systems large in size or configuration space, as a step towards accurate multiscale modeling.

CEs were successfully constructed for FCC binary and ternary bulk systems as well as binary FCC-(111) surfaces. This showcases the scalability of the method, in both increased number of components and decreased dimensionality. Based on these results, CEs of ternary surfaces, such as the full AuCuPd system, are within reach, and a possible extension is to study nanoparticles.

The constructed CEs were used to calculate the energy of atomic configurations during MC simulation, to obtain information about the ordering and segregation phenomena at different temperatures. For the AuPd system, results indicate complete miscibility in the bulk and a strong segregation of Au to the surface. At the surface, a tendency for ordering was observed, dominated by an Au_2Pd-phase. The characteristic phase separation of AuCu in bulk was observed, as well as segregation of Au to the surface. The AuCu surface consisted of both ordered regions and clustering of atoms. The CuPd system was found to be completely miscible in bulk, while the surface system showed unexpectedly strong ordering phenomena. Further modeling is needed to determine if this is a real phenomena or an error in the model. MC sampling of the full ternary bulk system was performed and phase separation with ordered phases at 50 and 33 %Cu was indicated.

An additional important finding is that in the systems studied, surface segregation tend to introduce an oscillation of concentration between the layers, such that the second layer compensates for the surface deficit, and the third layer compensates for the surplus of the second layer, and so forth. This is an important result since experimental measurements often lack the ability to target the surface layer only, which will lead to an underestimation of the segregation effect. For the AuPd and CuPd systems, this oscillation continues into the middle of the surface slabs, indicating that the slab thickness is not sufficient to get rid of surface effects in the core. In future studies, thicker slabs should be investigated to ensure that the surface atoms are not affected by the other surface.

This thesis provide several insights about the ordering and segregation in the PdAuCu system in vacuum. For the purpose of using PdAuCu nanoparticles for hydrogen sensing, future studies where the influence of adsorbates, such as H and CO, is encouraged.

Bibliography

[1] Hansan Liu et al. “A Review of Anode Catalysis in the Direct Methanol Fuel Cell”. en. In: *Journal of Power Sources* 155.2 (Apr. 2006), pp. 95–110. ISSN: 03787753. DOI: 10.1016/j.jpowsour.2006.01.030.

[2] Pablo Hervés et al. “Catalysis by Metallic Nanoparticles in Aqueous Solution: Model Reactions”. en. In: *Chemical Society Reviews* 41.17 (2012), p. 5577. ISSN: 0306-0012, 1460-4744. DOI: 10.1039/c2cs35029g.

[3] Antonino Salvatore Aricò et al. “Nanostructured Materials for Advanced Energy Conversion and Storage Devices”. En. In: *Nature Materials* 4.5 (May 2005), p. 366. ISSN: 1476-4660. DOI: 10.1038/nmat1368.

[4] Peter G. Bruce, Bruno Scrosati, and Jean-Marie Tarascon. “Nanomaterials for Rechargeable Lithium Batteries”. en. In: *Angewandte Chemie International Edition* 47.16 (2008), pp. 2930–2946. ISSN: 1521-3773. DOI: 10.1002/anie.200702505.

[5] Andrea Baldi et al. “In Situ Detection of Hydrogen-Induced Phase Transitions in Individual Palladium Nanocrystals”. en. In: *Nature Materials* 13.12 (Dec. 2014), pp. 1143–1148. ISSN: 1476-1122, 1476-4660. DOI: 10.1038/nmat4086.

[6] Carl Wadell et al. “Hysteresis-Free Nanoplasmonic Pd–Au Alloy Hydrogen Sensors”. In: *Nano Letters* 15.5 (May 2015), pp. 3563–3570. ISSN: 1530-6984. DOI: 10.1021/acs.nanolett.5b01053.

[7] Y. Volokitin et al. “Quantum-Size Effects in the Thermodynamic Properties of Metallic Nanoparticles”. en. In: *Nature* 384.6610 (Dec. 1996), pp. 621–623. ISSN: 0028-0836, 1476-4687. DOI: 10.1038/384621a0.

[8] Alexandre Albanese, Peter S. Tang, and Warren C.W. Chan. “The Effect of Nanoparticle Size, Shape, and Surface Chemistry on Biological Systems”. In: *Annual Review of Biomedical Engineering* 14.1 (2012), pp. 1–16. DOI: 10.1146/annurev-bioeng-071811-150124.

[9] Xiaochun Cao et al. “Effect of TiO 2 Nanoparticle Size on the Performance of PVDF Membrane”. en. In: *Applied Surface Science* 253.4 (Dec. 2006), pp. 2003–2010. ISSN: 01694332. DOI: 10.1016/j.apsusc.2006.03.090.

[10] T. Klar et al. “Surface-Plasmon Resonances in Single Metallic Nanoparticles”. en. In: *Physical Review Letters* 80.19 (May 1998), pp. 4249–4252. ISSN: 0031-9007, 1079-7114. DOI: 10.1103/PhysRevLett.80.4249.

[11] M. Pelton, J. Aizpurua, and G. Bryant. “Metal-Nanoparticle Plasmonics”. en. In: *Laser & Photonics Reviews* 2.3 (2008), pp. 136–159. ISSN: 1863-8899. DOI: 10.1002/lpor.200810003.

[12] Ferry Anggoro Ardy Nugroho et al. “Universal Scaling and Design Rules of Hydrogen-Induced Optical Properties in Pd and Pd-Alloy Nanoparticles”. In:

ACS Nano 12.10 (Oct. 2018), pp. 9903–9912. ISSN: 1936-0851. DOI: 10.1021/acsnano.8b02835.

[13] Iwan Darmadi et al. "Rationally Designed Binary and Ternary Alloy Nanoparticles for Poisoning-Resistant Nanoplasmonic Hydrogen Sensors with Hysterisis-Free Sub-Second Response". In: *Submitted for publication* (2019).

[14] J. J. Burton, E. Hyman, and D. G. Fedak. "Surface Segregation in Alloys". In: *Journal of Catalysis* 37.1 (Apr. 1975), pp. 106–113. ISSN: 0021-9517. DOI: 10.1016/0021-9517(75)90138-4.

[15] Mattias Ångqvist et al. "ICET – A Python Library for Constructing and Sampling Alloy Cluster Expansions". en. In: *Advanced Theory and Simulations* 0.0 (), p. 1900015. ISSN: 2513-0390. DOI: 10.1002/adts.201900015.

[16] Axel van de Walle. "Multicomponent Multisublattice Alloys, Nonconfigurational Entropy and Other Additions to the Alloy Theoretic Automated Toolkit". In: *Calphad*. Tools for Computational Thermodynamics 33.2 (June 2009), pp. 266–278. ISSN: 0364-5916. DOI: 10.1016/j.calphad.2008.12.005.

[17] J. M. Sanchez, F. Ducastelle, and D. Gratias. "Generalized Cluster Description of Multicomponent Systems". In: *Physica A: Statistical Mechanics and its Applications* 128.1 (Nov. 1984), pp. 334–350. ISSN: 0378-4371. DOI: 10.1016/0378-4371(84)90096-7.

[18] Richard M. Martin. *Electronic Structure : Basic Theory and Practical Methods*. Cambridge : Cambridge Univ. Press, 2004., 2004. ISBN: 978-0-521-78285-2.

[19] P. Hohenberg and W. Kohn. "Inhomogeneous Electron Gas". en. In: *Physical Review* 136.3B (Nov. 1964), B864–B871. ISSN: 0031-899X. DOI: 10.1103/PhysRev.136.B864.

[20] W. Kohn and L. J. Sham. "Self-Consistent Equations Including Exchange and Correlation Effects". en. In: *Physical Review* 140.4A (Nov. 1965), A1133–A1138. ISSN: 0031-899X. DOI: 10.1103/PhysRev.140.A1133.

[21] J. M. Thijssen. *Computational Physics*. Cambridge : Cambridge University Press, 2007., 2007. ISBN: 978-0-521-83346-2.

[22] Nicholas Metropolis et al. "Equation of State Calculations by Fast Computing Machines". en. In: *The Journal of Chemical Physics* 21.6 (June 1953), pp. 1087–1092. ISSN: 0021-9606, 1089-7690. DOI: 10.1063/1.1699114.

[23] R.K. Pathria. *Statistical Mechanics*. en. Butterworth-Heinemann, 1996. ISBN: 978-0-7506-2469-5. DOI: 10.1016/B978-0-7506-2469-5.X5000-2.

[24] Babak Sadigh and Paul Erhart. "Calculation of Excess Free Energies of Precipitates via Direct Thermodynamic Integration across Phase Boundaries". en. In: *Physical Review B* 86.13 (Oct. 2012). ISSN: 1098-0121, 1550-235X. DOI: 10.1103/PhysRevB.86.134204.

[25] Babak Sadigh et al. "Scalable Parallel Monte Carlo Algorithm for Atomistic Simulations of Precipitation in Alloys". en. In: *Physical Review B* 85.18 (May 2012), p. 184203. ISSN: 1098-0121, 1550-235X. DOI: 10.1103/PhysRevB.85.184203.

[26] Gus L. W. Hart and Rodney W. Forcade. "Algorithm for Generating Derivative Structures". en. In: *Physical Review B* 77.22 (June 2008), p. 224115. ISSN: 1098-0121, 1550-235X. DOI: 10.1103/PhysRevB.77.224115.

[27] Gus L. W. Hart and Rodney W. Forcade. "Generating Derivative Structures from Multilattices: Algorithm and Application to Hcp Alloys". en. In: *Physical Review B* 80.1 (July 2009), p. 014120. ISSN: 1098-0121, 1550-235X. DOI: 10.1103/PhysRevB.80.014120.

[28] G. Kresse and J. Hafner. "*Ab Initio* Molecular Dynamics for Liquid Metals". en. In: *Physical Review B* 47.1 (Jan. 1993), pp. 558–561. ISSN: 0163-1829, 1095-3795. DOI: 10.1103/PhysRevB.47.558.

[29] G. Kresse and J. Hafner. "*Ab Initio* Molecular-Dynamics Simulation of the Liquid-Metal–Amorphous-Semiconductor Transition in Germanium". en. In: *Physical Review B* 49.20 (May 1994), pp. 14251–14269. ISSN: 0163-1829, 1095-3795. DOI: 10.1103/PhysRevB.49.14251.

[30] G. Kresse and J. Furthmüller. "Efficient Iterative Schemes for *Ab Initio* Total-Energy Calculations Using a Plane-Wave Basis Set". en. In: *Physical Review B* 54.16 (Oct. 1996), pp. 11169–11186. ISSN: 0163-1829, 1095-3795. DOI: 10.1103/PhysRevB.54.11169.

[31] G. Kresse and J. Furthmüller. "Efficiency of Ab-Initio Total Energy Calculations for Metals and Semiconductors Using a Plane-Wave Basis Set". en. In: *Computational Materials Science* 6.1 (July 1996), pp. 15–50. ISSN: 09270256. DOI: 10.1016/0927-0256(96)00008-0.

[32] G. Kresse and D. Joubert. "From Ultrasoft Pseudopotentials to the Projector Augmented-Wave Method". en. In: *Physical Review B* 59.3 (Jan. 1999), pp. 1758–1775. ISSN: 0163-1829, 1095-3795. DOI: 10.1103/PhysRevB.59.1758.

[33] P. E. Blöchl. "Projector Augmented-Wave Method". en. In: *Physical Review B* 50.24 (Dec. 1994), pp. 17953–17979. ISSN: 0163-1829, 1095-3795. DOI: 10.1103/PhysRevB.50.17953.

[34] Ask Hjorth Larsen et al. "Libvdwxc: A Library for Exchange–Correlation Functionals in the vdW-DF Family". en. In: *Modelling and Simulation in Materials Science and Engineering* 25.6 (Sept. 2017), p. 065004. ISSN: 0965-0393, 1361-651X. DOI: 10.1088/1361-651X/aa7320.

[35] Rémi Marchal et al. "Structure of Pd/Au Alloy Nanoparticles from a Density Functional Theory-Based Embedded-Atom Potential". en. In: *The Journal of Physical Chemistry C* 117.42 (Oct. 2013), pp. 21810–21822. ISSN: 1932-7447, 1932-7455. DOI: 10.1021/jp4061686.

[36] X. W. Zhou, R. A. Johnson, and H. N. G. Wadley. "Misfit-Energy-Increasing Dislocations in Vapor-Deposited CoFe/NiFe Multilayers". en. In: *Physical Review B* 69.14 (Apr. 2004), p. 144113. ISSN: 1098-0121, 1550-235X. DOI: 10.1103/PhysRevB.69.144113.

[37] Steve Plimpton. "Fast Parallel Algorithms for Short-Range Molecular Dynamics". In: *Journal of Computational Physics* 117.1 (Mar. 1995), pp. 1–19. ISSN: 0021-9991. DOI: 10.1006/jcph.1995.1039.

[38] Weiming Huang et al. "Thermodynamic Modelling of the Cu–Pd–H System". en. In: *Calphad* 31.3 (Sept. 2007), pp. 315–329. ISSN: 03645916. DOI: 10.1016/j.calphad.2007.02.002.

[39] J. Magnus Rahm and Paul Erhart. "Understanding Chemical Ordering in Bimetallic Nanoparticles from Atomic-Scale Simulations: The Competition between Bulk, Surface, and Strain". en. In: *The Journal of Physical Chem-*

istry C 122.49 (Dec. 2018), pp. 28439–28445. ISSN: 1932-7447, 1932-7455. DOI: 10.1021/acs.jpcc.8b10874.

[40] A. V. Ruban, H. L. Skriver, and J. K. Nørskov. "Surface Segregation Energies in Transition-Metal Alloys". en. In: *Physical Review B* 59.24 (June 1999), pp. 15990–16000. ISSN: 0163-1829, 1095-3795. DOI: 10.1103/PhysRevB.59.15990.

[41] A. Christensen et al. "Phase Diagrams for Surface Alloys". en. In: *Physical Review B* 56.10 (Sept. 1997), pp. 5822–5834. ISSN: 0163-1829, 1095-3795. DOI: 10.1103/PhysRevB.56.5822.

A

VASP INCAR files

INCAR file used during relaxation:

```
ADDGRID = .TRUE.
AGGAC = 0.0
ALGO = Normal
AMIN = 0.01
AMIX = 0.05
EDIFF = 1e-06
EDIFFG = -0.01
ENCUT = 400
GGA = CX
IBRION = 1
ISIF = 2
ISMEAR = 1
KPAR = 2
LCHARG = .FALSE.
LREAL = .FALSE.
LUSE_VDW = .TRUE.
LWAVE = .FALSE.
NELM = 120
NPAR = 2
NSIM = 1
NSW = 40
PREC = Accurate
SIGMA = 0.1
SYMPREC = 1e-08
```

INCAR file used during final energy calculation:

```
ADDGRID = .FALSE.
AGGAC = 0.0
ALGO = Normal
AMIN = 0.01
AMIX = 0.05
EDIFF = 1e-06
ENCUT = 400
ENMAX = 40
ENMIN = -20
GGA = CX
ISIF = 0
ISMEAR = -5
KPAR = 2
LCHARG = .FALSE.
LORBIT = 11
LREAL = .FALSE.
LUSE_VDW = .TRUE.
LWAVE = .FALSE.
NEDOS = 1201
NELM = 120
NPAR = 2
NSIM = 1
NSW = 0
PREC = Accurate
SIGMA = 0.05
SYMPREC = 1e-08
```